High Resolution Spectroscopy Across the Hot Jupiter Regime

Abhiram Bibekar
Part III Astrophysics Project Report
Supervised by Prof. Nikku Madhusudhan

May 2022

Abstract

The abundance of high-resolution spectroscopic observations of exoplanet atmospheres has allowed for a revolution in our understanding of their properties and processes. In this report, we develop a pipeline to analyse archival transit observation of the hot Jupiters HD 189733b, WASP 121b and WASP 79b. We apply this pipeline to extract the respective transmission spectra for each target, carefully correcting for telluric features, and robustly confirm the detections of atomic sodium in the optical to $> 3.8\sigma$. Individually resolving the Na D1 and D2 lines with Gaussian profiles, we interpret the line depth, position and full width at half maximum (FWHM) to make inferences about the nature of each target atmosphere. A comparative analysis is performed to contextualise the detections with other sodium detections in the literature and to identify possible population trends.

1 Introduction

The study of extrasolar planets, or exoplanets, has come a long way since the discovery of 51 Pegasi b in 1995 (Mayor and Queloz 1995) - the first exoplanet to be found orbiting a main sequence star. The confluence of significant advances in observational techniques, computational resources, and the quality and quantity of observations has taken the field to over 5000 confirmed exoplanet detections at the time of writing (NASA Exoplanet Archive 2022). Through this journey, it has become clear our solar system represents but a small fraction of the full diversity manifest in the exoplanetary zoo: for example over 1500 super-Earths (exoplanets more massive than Earth but lighter than Neptune) have been discovered (NASA Exoplanet Archive 2022) but find no clear analogue within our solar system. Considering bulk planetary parameters, our solar system spans equilibrium temperatures, masses and radii of $\sim$50 K to 500 K, $\sim$1 $M_\oplus$ to 320 $M_\oplus$, and $\sim$1 $R_\oplus$ to 11 $R_\oplus$ and exhibits a plethora of planetary processes; the fact exoplanets span an even wider space of $\sim$200 K to 4000 K, $\sim$1 $M_\oplus$ to 1×10^4 $M_\oplus$ and $\sim$0.5 $R_\oplus$ to 20 $R_\oplus$ (Madhusudhan 2019) means their study allows us to shed light on physical processes at the extremes, and to perhaps begin to answer questions at the scientific frontier regarding the formation and evolution of planetary systems. With this in mind, this work focuses on a sample of three exoplanets across the hot Jupiter exoplanet class and investigates planetary properties, processes and population trends.

1.1 Hot Jupiters

The hot Jupiters are a class of exoplanets with two defining characteristics: they are gas giants physically akin to Jupiter, but located very close to their host stars with orbital separations $a \sim 0.1$ au. They are readily detected by measuring the oscillations induced in the motion of their host stars, given their high mass and very short periods, meaning they are somewhat overrepresented in the current detection landscape. Most follow nearly circular orbits and exhibit perfect tidal locking which introduces a permanent dayside and nightside. Given the very high incident stellar flux, the daysides temperatures vary from 1600 K to 4000 K, making hot Jupiters excellent laboratories for study of processes under extreme conditions. Observations have uncovered details of thermal inversions (Haynes et al. 2015; Evans et al. 2017)and atmospheric escape (Ehrenreich et al. 2015; F. Yan and Henning 2018) for example. The high temperatures also allow many chemical species to be present within the atmosphere, with molecular detection examples including H_2O (Birkby et al. 2013), CO (Snellen et al. 2010; Brogi et al. 2012) and TiO (Nugroho et al. 2017), and atomic examples including Mg, Ti, Ca and Fe (Hoeijmakers et al. 2019; Ben-Yami et al. 2020; Casasayas-Barris, Pallé, et al. 2019). The most readily predicted and detected species are the alkali metals Na and K due to their large optical absorption cross sections with numerous groups (Redfield et al. 2008; Charbonneau et al. 2002; Sedaghati et al. 2016; Wyttenbach et al. 2015; Casasayas-Barris, Palle, et al. 2017; Hoeijmakers et al. 2019; Cabot et al. 2020) reporting successful detections across the Hot Jupiter regime. We focus on detecting sodium through the D2 and D1 absorption lines at 5889.951 Å and 5895.924 Å for our sample of planets.

1.2 Exoplanetary atmospheres

As the visible outer, partially transparent shell encasing a planet's interior, planetary atmospheres offer an unparalleled window into the various physical and chemical processes occurring both in the atmosphere itself and within the planet's interior. These processes encode a vast array of information pertaining to the formation and evolutionary history of the planet, and indeed potential habitability and signs of life, making them a fertile ground for scientific discovery.

The primary vehicle for characterisation of exoplanetary atmospheres is spectroscopy. Spectroscopic observations of the exoplanet's atmosphere during transit contain a variety of markers and signals from the interaction of light with species within the atmosphere. In the lower atmosphere, chemical equilibrium and low temperatures mean molecules such as H_2O, CO_2, and CH_4 are present in high quantities; these species introduce strong absorption features in the infrared from rotovibrational transitions. Higher up, non-equilibrium processes begin to dominate and elevated temperatures induce chemical decomposition - as such the key markers become atomic elements, such as Na, K and Fe, and high temperature refractory species e.g. TiO and VO. These species have strong absorption cross sections within the optical; indeed for the refractory species this can introduce thermal inversions due to the thermospheric heating from the absorbed stellar flux. In the upper regions of the atmosphere, spectral signatures are more muted due to the thinness of the atmosphere, but some features are visible within the UV from photochemical dissociation reactions induced by the high levels of XUV stellar flux. Crucially, all the properties of the spectral features are also influenced by the local atmospheric conditions for the absorbing species (e.g. temperature, pressure, wind speed). Thus through inverse modelling and physical reasoning it is therefore possible to constrain these atmospheric conditions from spectral features; this forms the basis of the work in latter half of this project.

1.3 High-resolution ground-based transit spectroscopy

How are these spectroscopic observations performed? There are two main types of observations, corresponding to different points in orbital phase. The first type is emission spectroscopy, where observations are made just before and during secondary eclipse of the planet. The former observations contain the sum of the stellar and planetary flux, and the latter contain just the stellar flux - thus by dividing out the latter spectra from the former it is possible to recover the emission spectrum of the planet dayside through the atmosphere. Emission spectroscopy primarily probes the temperature structure of the dayside atmosphere and lower atmosphere chemical composition.

The second type is transmission spectroscopy, where observations are made while the planet is transiting the host star. Again, to recover the transmission spectrum these observations are divided by the stellar spectrum using out-of-transit observations. In this geometry we measure the atmosphere through

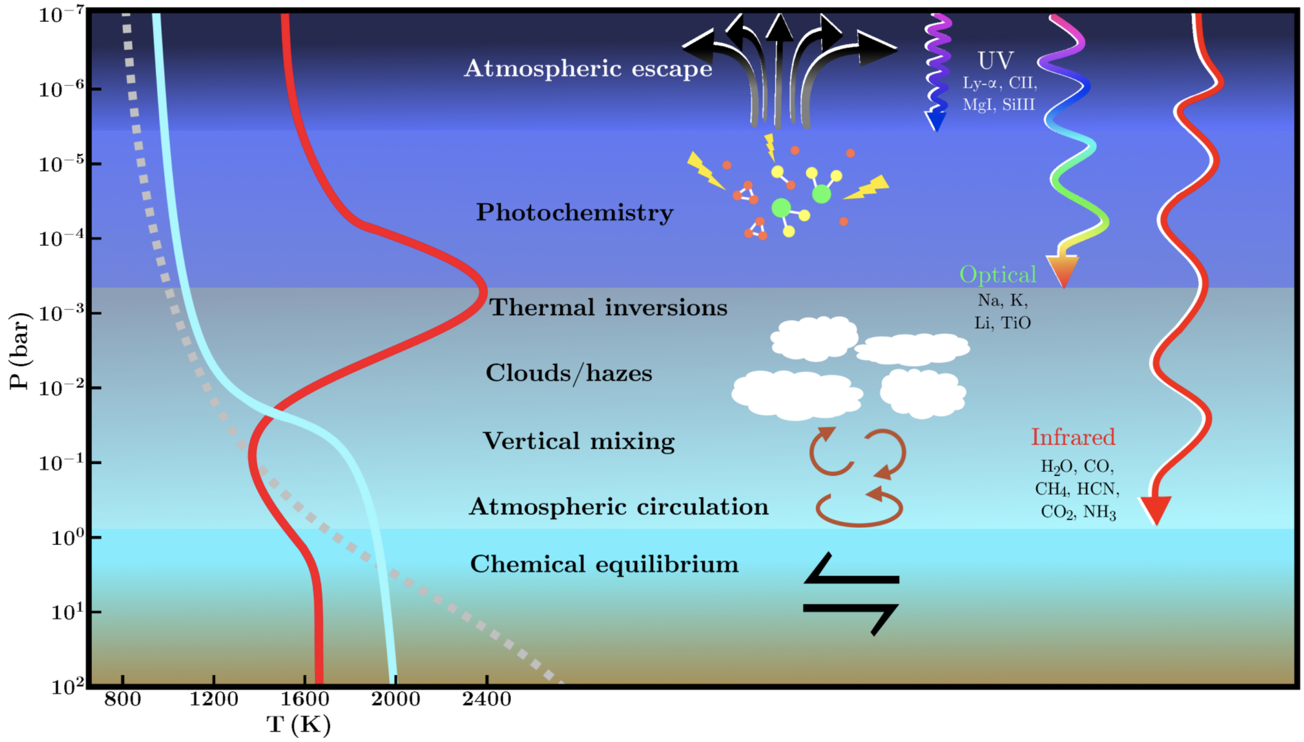

Figure 1: Atmospheric processes at different levels of the atmosphere, and the corresponding wavelength regions containing information on these processes (Madhusudhan 2019).

the planet day-nightside terminator i.e. through a cross section of the atmosphere perpendicular to the line of sight. Transmission spectroscopy therefore provides information on the chemical composition and local properties of the upper atmosphere. For this project, we focus on transmission spectroscopy since at high resolution this presents the opportunity to individually resolve the D2 and D1 sodium lines, and thus measure their line profile characteristics to infer local atmospheric conditions.

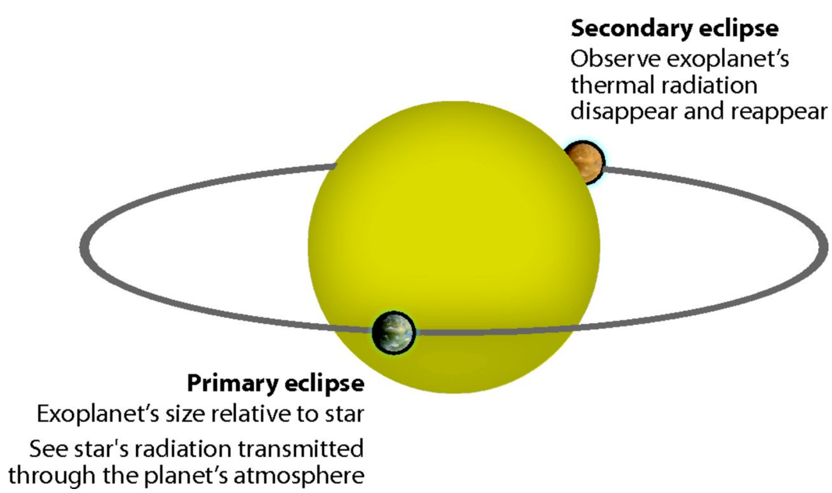

Figure 2: Illustration of the two observation geometries: primary eclipse corresponding to transmission spectroscopy, and secondary eclipse corresponding to emission spectroscopy. (Seager and Bains 2015)

There are a number of practical challenges in using transmission spectroscopy to probe exoplanet atmospheres. We must first ensure enough observations are made bracketting the planet transit since developing a strong out-of-transit baseline to subtract the stellar spectrum from in-transit observations is crucial to recovering an accurate planetary transmission spectrum (Wyttenbach et al. 2015). Capturing the sodium absorption fine structure at high resolution is currently only possible with ground-based observations through large aperture telescopes, which presents the most significant challenge: removal of contamination of the spectra due to absorption from the Earth's atmosphere. Telluric lines in the optical, predominantly due to H_2O and O_2, can merge with stellar lines or introduce spurious features into the transmission spectrum (A. B. Langeveld et al. 2021) so it is essential to perform an accurate telluric correction - details of how this was achieved are covered in subsection 2.3. An addition challenge is accounting for the stellar reflex motion, systemic velocity and planetary radial velocity during observations; Wyttenbach et al. 2015 highlights how the not accounting for the latter in particular can detrimentally impact detection results.

1.4 Project aims

Current work at the frontier of exoplanetary science has moved past detection and analysis of individual planets to focus on comparative characterisation of ensembles of planets to recover broader trends within exoplanet categories (Crossfield and Kreidberg 2017; Welbanks et al. 2019; Wallack et al. 2019; Changeat et al. 2022; A. Langeveld, Madhusudhan, and Cabot 2022). Identification of such trends could provide a starting point for novel theories explaining the processes at play within atmospheres, as well as a provide constraints on planetary formation and evolution mechanisms. This project aims to contribute to this endeavour for the hot Jupiters through sodium detections and aims to answer three key questions:

1. What is the frequency and nature of alkali absorption for hot Jupiters?
2. What can the alkali detection tell us about the atmospheric properties of hot Jupiters?
3. How do atmospheric properties and processes vary across the hot Jupiter regime?

The structure of the project is as follows. Section 2 details the observational data chosen and the detection methodology, including details of the telluric corrections removal of the stellar spectra for the three targets chosen. Section 3 presents the resulting recovered planetary transmission spectra along with parameters characterising the observed Na D2 and D1 line profiles. Using these results, we perform a detailed analysis of a number of local atmospheric properties in Section 4 and identify a number of speculative trends within the data. In section 5 we examine the inferences made in the context of results within the literature and propose possible explanations for the trends observed. Concluding remarks are provided in Section 6.

2 Observations and data analysis

2.1 Observations of HD 189733b, WASP 79b, WASP 121b

In light of the aforementioned science goals of the project, we chose three exoplanets as our targets: HD 189733b, WASP 79b and WASP 121b. All three targets are well known hot Jupiters with a satisfactory number of high quality ground-based high-resolution spectroscopic observations available, thus permitting extraction of potential sodium features. The selection also presents the opportunity to perform a comparative analysis across the targets as they span a broad range of temperatures: the equilibrium temperatures $T_{\rm eq}$ for HD 189733b, WASP 79b and WASP 121b are measured to be 1220 K (Addison et al. 2019), 1716 K (Brown et al. 2017) and 2720 K (Mikal-Evans, Sing, Goyal, et al. 2019) respectively.

Table 1 summarises the archival spectra retrieved for each target from the European Southern Observatory (ESO) archive. For successful extraction of the planetary transmission spectrum, it is crucial to have a number of out-of-transit observations bracketing the transit to generate a strong out-of-transit baseline. Without this, it is difficult to recover the planetary transmission signal through subtraction of the out-of-transit baseline from the in-transit observations as the signal to noise ratio (SNR) is too low. From Figure 3 we see that this criteria is met for all observations barring night 0 for HD 189733b. Further inspection of the spectra for this night indicates fairly poor weather conditions; this combined with the limited number of observations prompts us to omit HD 189733b night 0 data from the rest of the project analysis.

All observations were made using the High Accuracy Radial velocity Planet Searcher (HARPS) echelle spectrograph at the ESO La Silla 3.6 m telescope. HARPS records 72 echelle spectrum orders which together span a range of 3700 Å to 6900 Å. Two fibres are employed in observations: fibre A, which observes the actual target; and fibre B, which either records a ThAr spectrum or night sky spectrum for calibration. The raw observations are automatically calibrated and remapped to a uniform 0.01 Å one-dimensional grid in the solar system barycentric rest frame by the HARPS Data Reduction Software (DRS) v3.5.

We can heuristically determine the quality of the data for each target by assuming the error in the flux values to be dominated by photon noise (i.e. $\sim \sqrt{\mathrm{flux}}$) and considering the number of nights of observations available. Anticipating that for each target we produce a transmission spectrum for each night of observation and then combine these into a single average transmission spectrum across nights using inverse variance weighting, the SNR of the final combined spectrum for each target should scale as $\sim \sqrt{\mathrm{N_{nights}}/\mathrm{flux}}$. The fluxes for WASP 79b and WASP 121b are similar; the fluxes for HD 189733b are $\sim 2.3\times$ higher. This leads us to conclude that HD 189733b has the highest quality observational data and WASP 79b the worst.

Planet	Night	Date	#In	#Out	#Other	Program ID
HD 189733b	0	2006-07-29	5	6	1	072.C-0488(E)
	1	2006-09-07	10	8	2	072.C-0488(E)
	2	2007-07-19	19	19	1	079.C-0828(A)
	3	2007-08-28	19	19	2	079.C-0127(A)
WASP 79b	0	2012-11-12	22	5	2	090.C-0540(H)
WASP 121b	0	2017-12-31	14	19	2	0100.C-0750(C)
	1	2018-01-09	19	34	2	0100.C-0750(C)
	2	2018-01-14	19	30	1	0100.C-0750(C)

Table 1: Summary of HARPS archival observations. The number of in-transit, out-of-transit and ingress/egress frames are calculated by using the system parameters from the NASA Exoplanet Archive along with the `DATE OBS` and `EXP TIME` fields in the `s1da` file headers. PIs: Mayor for 072.C-0488(E), 079.C-0828(A); Lecavelier des Etangs for 079.C-0127(A); Triaud for 090.C-0540(H); Ehrenreich for 0100.C-0750(C).

2.2 Data reduction

Each observation consists of a `s1d` file containing a single array: the flux over a range 3781 Å to 6912 Å measured at each 0.01 Å pixel. The corresponding flux errors are assumed be photon-noise limited ($\sim \sqrt{\mathrm{flux}}$). We first truncate this array to a range of 4000 Å to 6800 Å since strong telluric absorption and low throughput introduce large systematic effects at the edges of spectra. A number of pixels have anomalously high flux values; we identify these by creating a mask spectrum by applying a 9 pixel wide

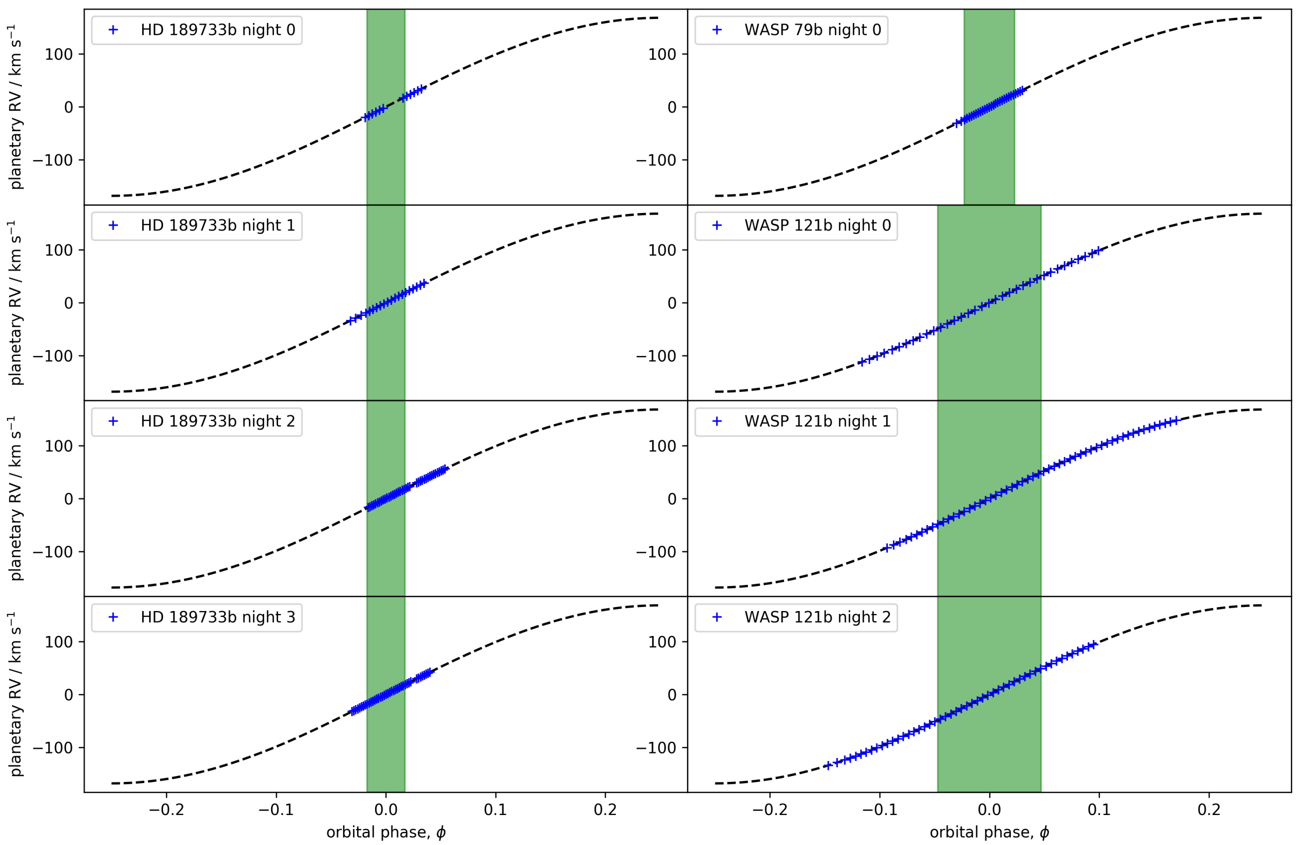

Figure 3: Planetary radial velocity (RV) curves with orbital phase for the observational dataset. The dashed line shows the modelled RV curve using the system parameters from the NASA Exoplanet Archive and the blue crosses represent the observations. The green highlighted regions indicate the transit window i.e. the time between first and fourth contact.

median filter and subtracting this from the original spectrum. Pixels with flux values which are $> 10\sigma$ from the median are designated as anomalous, and we replace the original flux values with the median from the 10 surrounding pixels. Finally, each spectrum is normalised by dividing by the spectrum median flux. Throughout this procedure, we ensure to propagate the uncertainties from photon noise throughout the analysis. All spectra are saved as `FITS BinTables` using the `astropy` package with the original metadata preserved in the header, and with arrays containing the wavelength grid, flux values and flux errors.

2.3 Telluric correction

We now perform the telluric correction: the most challenging part of the data reduction process. For detection of atmospheric sodium, we are most interested in the visible region of the spectra around ~ 5800 Å. The dominant telluric contaminants in this region are O_2 and H_2O, which impose features of the form shown in Figure 4 on ground-based spectroscopic observations. The difficulty in telluric correction arises from the time-varying nature of these features: since the Earth's atmosphere is a dynamic and highly complex system, the strength and profile of the features vary significantly over an intra- and inter-night basis. Our corrections for these effects must thus take into account the nuances of each observation, and incorporate the limited weather information included within each spectrum and its metadata. Multiple approaches feature within the literature for corrections in the optical regime, with some notable example including: deriving a telluric spectrum from the data alone using the assumption that the telluric feature strength varies linearly with airmass (Wyttenbach et al. 2015; Vidal-Madjar et al. 2010; Astudillo-Defru and Rojo 2013); applying radiative transfer models of the Earth's atmosphere to generate a synthetic telluric spectrum using codes such as `TERRASPEC` (Lockwood et al. 2014) and `molecfit` (Smette et al. 2015; Kausch et al. 2015); and applying Gaussian Processes to model the telluric signals (Meech et al. 2022).

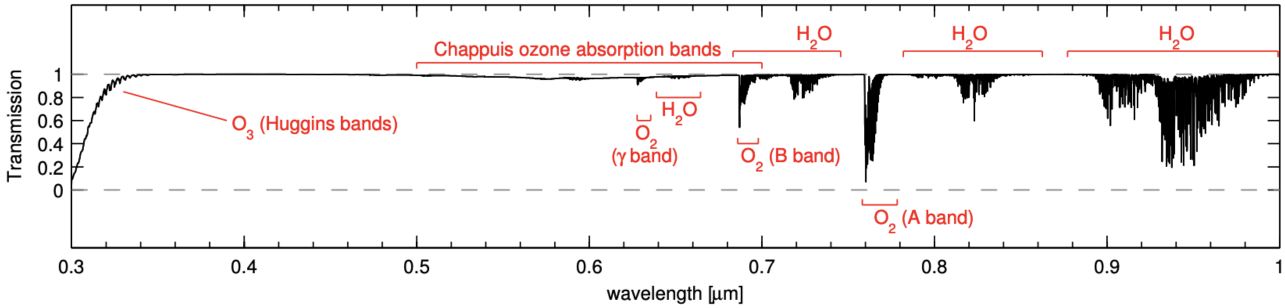

Figure 4: A synthetic example of the absorption spectrum of sky over 0.3 µm to 1.0 µm calculated using LBLRTM (Clough et al. 2005) using the annual mean atmospheric profile for Cerro Paranal. Reproduced from Smette et al. 2015.

We choose to proceed with the `molecfit` approach. The reasons for this follow from A. B. Langeveld et al. 2021 which provides an empirical comparison of the performance of `molecfit` to the "linear-airmass method". In their work, the authors conclude `molecfit` provides atomic detections at higher significance level (due to better telluric feature removal), introduces a lower level of detection variability across different nights for a single target, and can cope better with poorer quality data (e.g. a limited number of out-of-transit observations or high intra-night weather variation). This final point is worth emphasising as a general advantage of modelling-based approaches over data-driven approaches: the latter relies on having a number of spectra available to perform the regression, and thus has an efficacy which scales with the number and quality of the observations within the dataset. This decision is further justified by the state-of-the-art reported accuracy of `molecfit` corrections of 2% of the continuum flux level or better (Smette et al. 2015).

How does `molecfit` work? The program requires a number of data inputs: the spectrum to be corrected in `FITS BinTable` format (i.e. arrays with the wavelength grid, flux values and (optionally) the flux errors) in the telescope's reference frame; the spectrum metadata, which contains details of the weather conditions at time of observation; and a series of "include regions" for the fitting procedure. With the weather condition measurements and archived regional atmospheric profiles (data for variation of temperature, pressure and H_2O, O_2 abundances with altitude), an approximate combined atmospheric profile is generated. This provides the basis for an initial telluric spectrum to be generated using a line-by-line radiative transfer model, LBLRTM (Clough et al. 2005). Through comparison of this spectrum to the actual observation spectrum over small wavelength ranges where telluric lines dominate (i.e. the "include regions"), the H_2O and O_2 profiles are varied iteratively until the quality of the fit of the synthetic spectrum falls below a specified reduced χ^2 tolerance. The telluric correction is performed by dividing each observation by its best-fit telluric spectrum.

To prepare our data for `molecfit`, we first convert all spectra from the solar system barycentric reference frame to the telescope reference frame using the barycentric Earth radial velocity (BERV)

v_{BERV} (reported in observation metadata) to apply a Doppler shift to wavelength array:

$$\lambda_{\mathrm{HARPS}} = \sqrt{\frac{c + v_{\mathrm{BERV}}}{c - v_{\mathrm{BERV}}}} \lambda_{\mathrm{bary}}. \tag{1}$$

We then specify around fifteen ~ 2 Å wide include regions for each night of observations. This is accomplished by overplotting a generic telluric spectrum with a sample of observations for a given night and selecting (by eye) regions which contain telluric lines only; selecting a region with partial stellar or planetary absorption would severely compromise the quality of the telluric correction. This process required significant attempts to find the correct balance between undercorrection and overcorrection. An example of the include regions selected is depicted in Figure 5. Finally, we package the data inputs with the program parameters into a overall parameter file for each observation, ready to be supplied to `molecfit`.

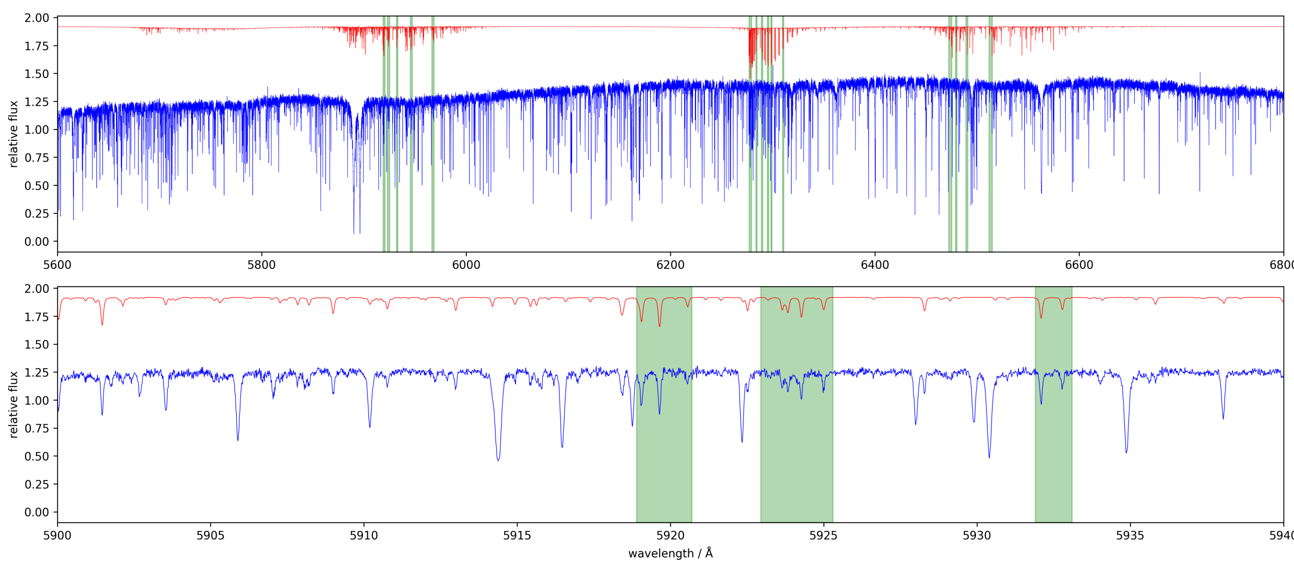

Figure 5: Top: Plot showing example HD 189733b night 0 observation spectrum (blue) with generic telluric spectrum (red) offset vertically for clarity. Selected include regions are shaded green. The telluric absorption at ~5900 Å and ~6500 Å are from H_2O, ~6300 Å is from O_2. Bottom: Same plot as top but over 5900 Å to 5940 Å to show how include regions are chosen to only contain telluric features.

Figure 6 depicts an example spectrum pre- and post-correction along with corresponding uncertainties. Similar plots across the whole dataset confirm that `molecfit` successfully reduced all telluric features down to the continuum noise level as required.

2.4 Extraction of transmission spectrum

After the removal of telluric features, we have a set of out-of-transit spectra $\{f(\lambda, t_{\mathrm{out}})\}$ and in-transit spectra $\{f(\lambda, t_{\mathrm{in}})\}$; the former should contain observations of the stellar spectrum alone at different times, while the latter should contain combined observations of the stellar and planetary spectra. To recover the planetary spectrum, we begin by first moving all spectra back into the solar system barycentric reference frame. We then move each spectrum into the stellar reference frame by applying a Doppler shift using $v_\star$:

$$v_\star = K_\star \sin(2\pi\phi) + v_{\mathrm{sys}} \tag{2}$$

where $K_\star$ is the stellar RV semi-amplitude, ϕ the orbital phase of the observation, and v_{sys} the systemic velocity. We opt to use modelled values for $v_\star$ as the velocities reported in the spectra metadata are

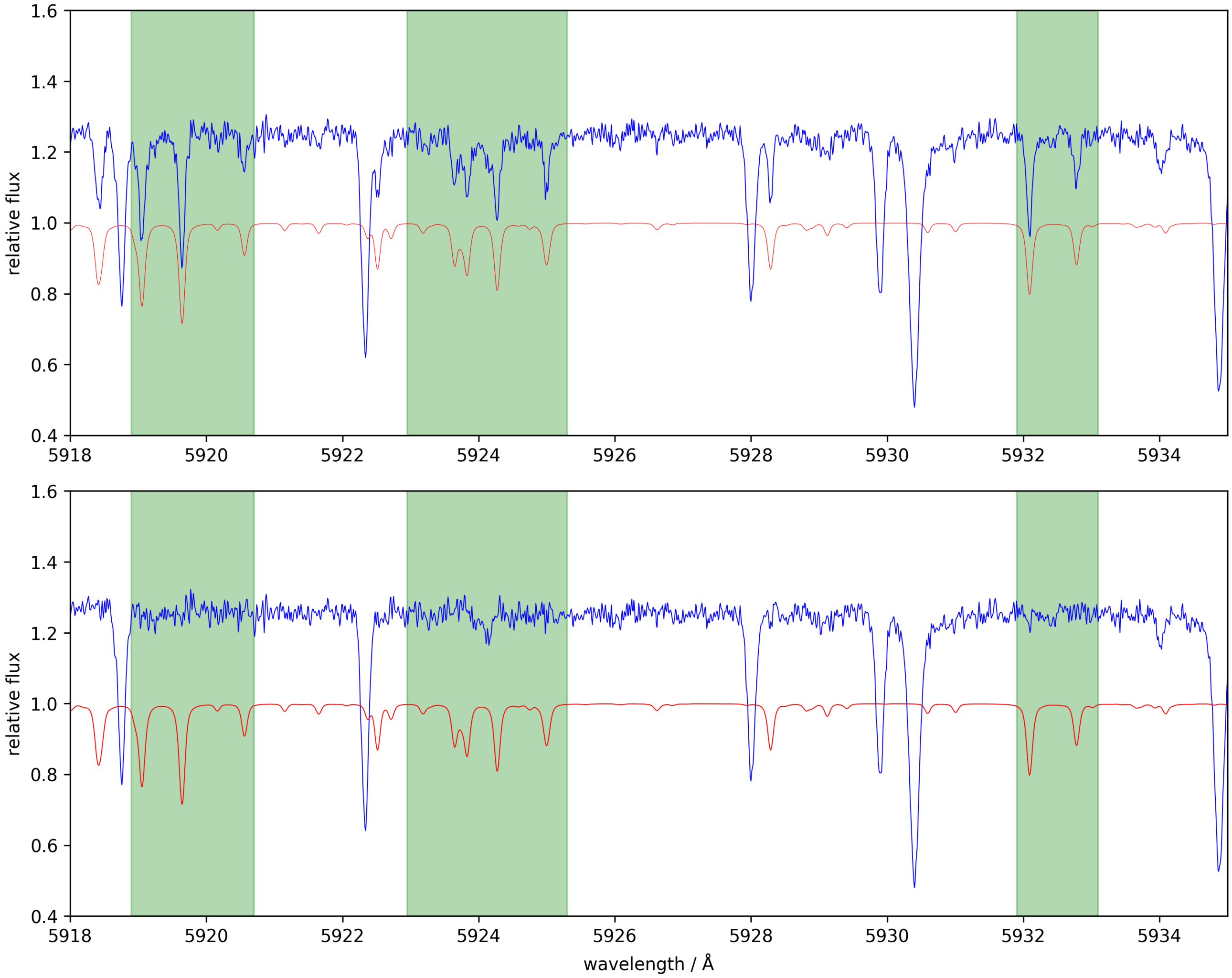

Figure 6: Plot showing example HD 189733b night 0 observation spectrum (blue) prior to telluric correction (top) and after correction (bottom). Corresponding telluric spectrum overplotted in red. Include regions are shaded green.

not well measured due to low SNR, particularly for some of the WASP 79b and WASP 121b observations. The most $v_\star$ was found to vary by was $300\,\mathrm{m\,s^{-1}}$, which corresponds to a shift by $\sim 6 \times 10^{-3}$ Å. After linearly interpolating the out-of-transit spectra onto a common 0.01 Å grid, a master out-of-transit spectrum $\bar{f}_{\mathrm{out}}(\lambda)$ (corresponding to the pure stellar spectrum) can be produced through co-addition i.e. performing an average across $\{t_{\mathrm{out}}\}$ weighted by the inverse variance - this maximises the SNR of the result and limits the impact of spectra affected by poor weather conditions.

The master out-of-transit spectrum $\bar{f}_{\mathrm{out}}(\lambda)$ is divided out from $\{f(\lambda, t_{\mathrm{in}})\}$ to produce a set of pure planetary transmission spectra $\{\mathfrak{R}(\lambda, t_{\mathrm{in}})\}$. Each $\mathfrak{R}(\lambda, t_{\mathrm{in}})$ is continuum normalised by a third degree polynomial fit to remove any lingering systematics or weather variation. A final Doppler shift into the planetary reference frame is applied using v_p, where $v_p = K_p \sin(2\pi\phi)$ and K_p is the planetary RV semi-amplitude. The most v_p was found to vary by was $\sim 200\,\mathrm{km\,s^{-1}}$, which corresponds to a shift by ~ 3 Å which highlights the importance of performing this step. We once again combine the spectra using an inverse variance weighted average across $\{t_{\mathrm{out}}\}$ to produces $1 + \mathfrak{R}'(\lambda)$, where $\mathfrak{R}'(\lambda)$ is the final combined planetary transmission spectrum as required.

3 Results: transmission spectra and line properties

3.1 Transmission spectra

Figure 7 depicts the final combined (across all nights) transmission spectra obtained for the three targets: HD 189733b, WASP 79b and WASP 121b. For all three targets, the sodium D2 line feature is visible by eye at $\lambda \approx 5890\,\text{Å}$. Relative to the continuum, the D2 feature is most clearly visible for HD 189733b; for WASP 79b and WASP 121b it is less well defined. Particularly for WASP 79b, there is a greater level of variation in the continuum signal around the D2 and D1 lines - this is likely due to limited number of observations available for this target, which limits how much these artefacts can be averaged out. For the D1 feature, identification by eye is only really possible for HD 189733b. The signal is hard to identify for WASP 79b due to the high continuum variation; for WASP 121b the feature itself appears to be wide and of low amplitude, which reduces its visibility.

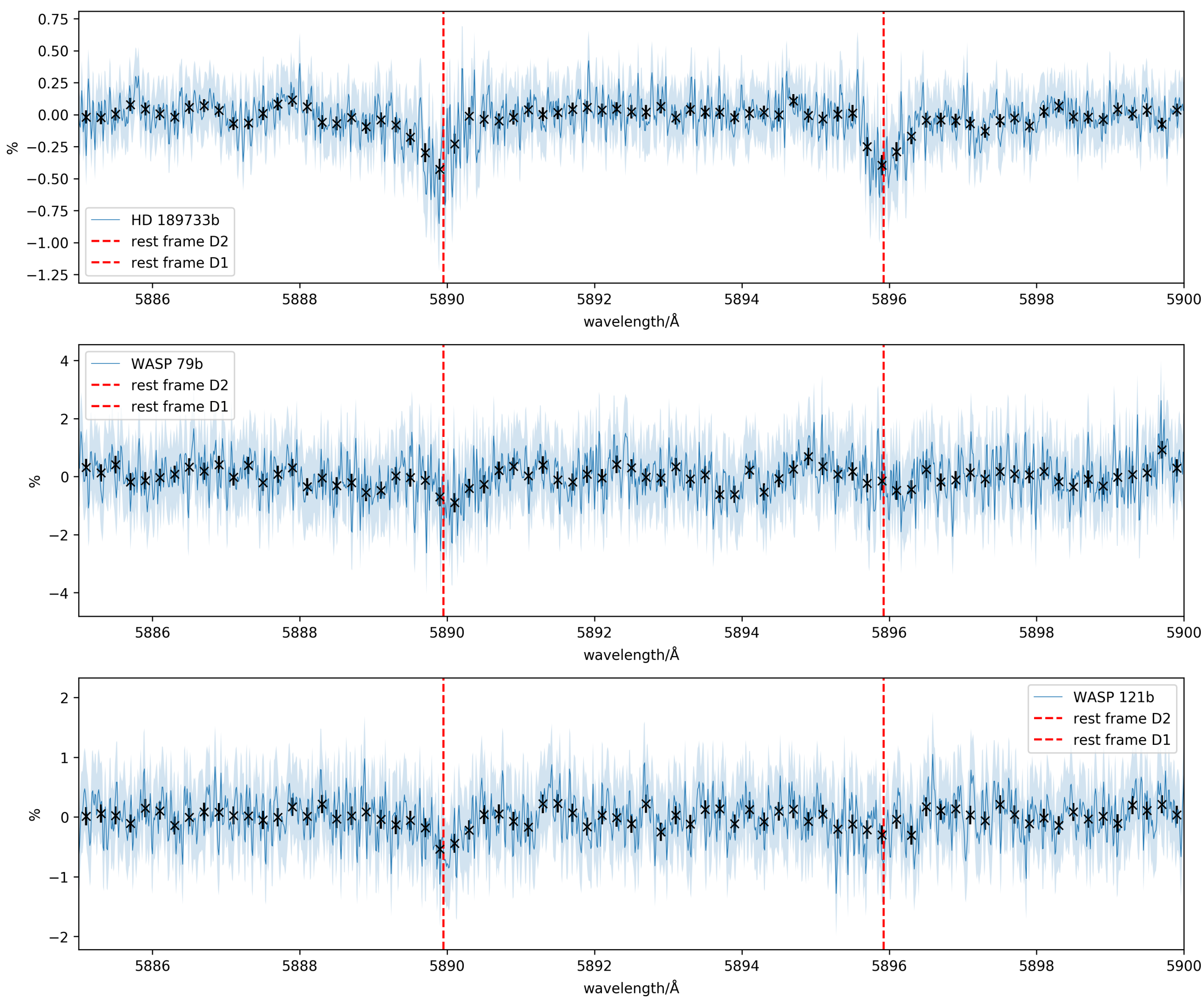

Figure 7: Final combined transmission spectra for each target over sodium doublet region. Black crosses are 20x binning of spectra. Red dashed lines indicate the lab rest frame positions of the D2 and D1 lines.

Comparing each spectrum to the corresponding telluric spectrum shows limited remaining telluric absorption features. This is further confirmed at a night-by-night level. There are a few small regions elevated above the continuum level where `molecfit`may have overcorrected the spectra, but the impact of these artefacts is insignificant due to their small relative amplitude. Further iterations of `molecfit` corrections adapting the specified "include regions" to add more telluric lines and over the artifact regions, as well as varying the "include regions" within the observing nights themselves are likely to yield more accurate corrections and further limit the presence of artefacts, but were deemed beyond the requirements of the remaining project analysis.

3.2 Fitting Gaussian line profiles

To isolate and better characterise the sodium doublet we fit Gaussian line profiles to the D2 and D1 lines individually for each target. In theory, the full line profiles follow a Voigt function, which is the convolution of the Gaussian and Lorentzian profiles. This is due to two effects: thermal Doppler broadening which introduces a Gaussian broadening of the original transition line; and pressure broadening which further imposes a Lorentzian profile. To good approximation however, it is found that a Gaussian profile well models the line cores, so we proceed as such. To perform the fitting procedure we make use of the `astropy` implementation of the Levenberg-Marquardt algorithm, which performs a least-squares fit to the data accounting for the flux errors. The fits are performed over 0.3 Å wide regions of the spectra centred on the lab frame line positions of 5889.951 Å and 5895.924 Å for the D2 and D1 lines respectively. We calculate the quality of each fit using a reduced chi squared metric χ^2_ν and estimate the uncertainties in the fit parameters from the covariance matrix included in the fitting procedure results. The resulting Gaussian fits are shown in Figure 8 and summarised in Table 2.

target	line	mean, Å	depth, %	FWHM, Å	χ^2_ν
HD 189733b	D2	5889.83 ± 0.02	0.38 ± 0.03	0.64 ± 0.05	0.296
HD 189733b	D1	5895.953 ± 0.019	0.44 ± 0.04	0.48 ± 0.04	0.305
WASP 79b	D2	5890.05 ± 0.03	1.01 ± 0.16	0.44 ± 0.08	0.263
WASP 79b	D1	5896.17 ± 0.04	0.72 ± 0.19	0.28 ± 0.09	0.256
WASP 121b	D2	5889.98 ± 0.03	0.60 ± 0.07	0.44 ± 0.06	0.229
WASP 121b	D1	5895.76 ± 0.09	0.25 ± 0.5	0.83 ± 0.21	0.248

Table 2: Summary of homogeneous Gaussian fit results.

The resultant fit parameters (line position, depth and FWHM) prove to be comparable to similar results in the literature. For HD 189733b, A. B. Langeveld et al. 2021 reports 5889.87 ± 0.03 Å, -0.64 ± 0.07 % and 0.46 ± 0.04 Å for the D2 line, and 5895.93 ± 0.04 Å, -0.53 ± 0.07 % and 0.42 ± 0.04 Å for the D1 line. Wyttenbach et al. 2015 reports line depth of -0.64 ± 0.07 % (D2) and -0.40 ± 0.07 % (D1), and FWHM for D2 and D1 both of 0.52 ± 0.08 Å. For D1 feature all three parameters are in good agreement with the literature values; for the D2 line there is good agreement on the line position but poor agreement on the depth and width. A. Langeveld, Madhusudhan, and Cabot 2022 indicates this discrepancy is likely due to differences in data reduction: previous measurements (Wyttenbach et al. 2015; A. B. Langeveld et al. 2021) appear to to combine the spectra without inverse-variance weighting, whereas this work combines with inverse-variance weighting. Revised results (with inverse-variance weighting) from A. Langeveld, Madhusudhan, and Cabot 2022 for the line depth are -0.39 ± 0.06 % for both the D2 and D1 lines, which are at 1σ agreement with the values measured in this work.

For WASP 79b, the only detection in the literature is A. Langeveld, Madhusudhan, and Cabot 2022 which reports line depths of -1.12 ± 0.23 % (D2) and -0.85 ± 0.22 % (D1). This is in 1σ agreement with the values measured in this work.

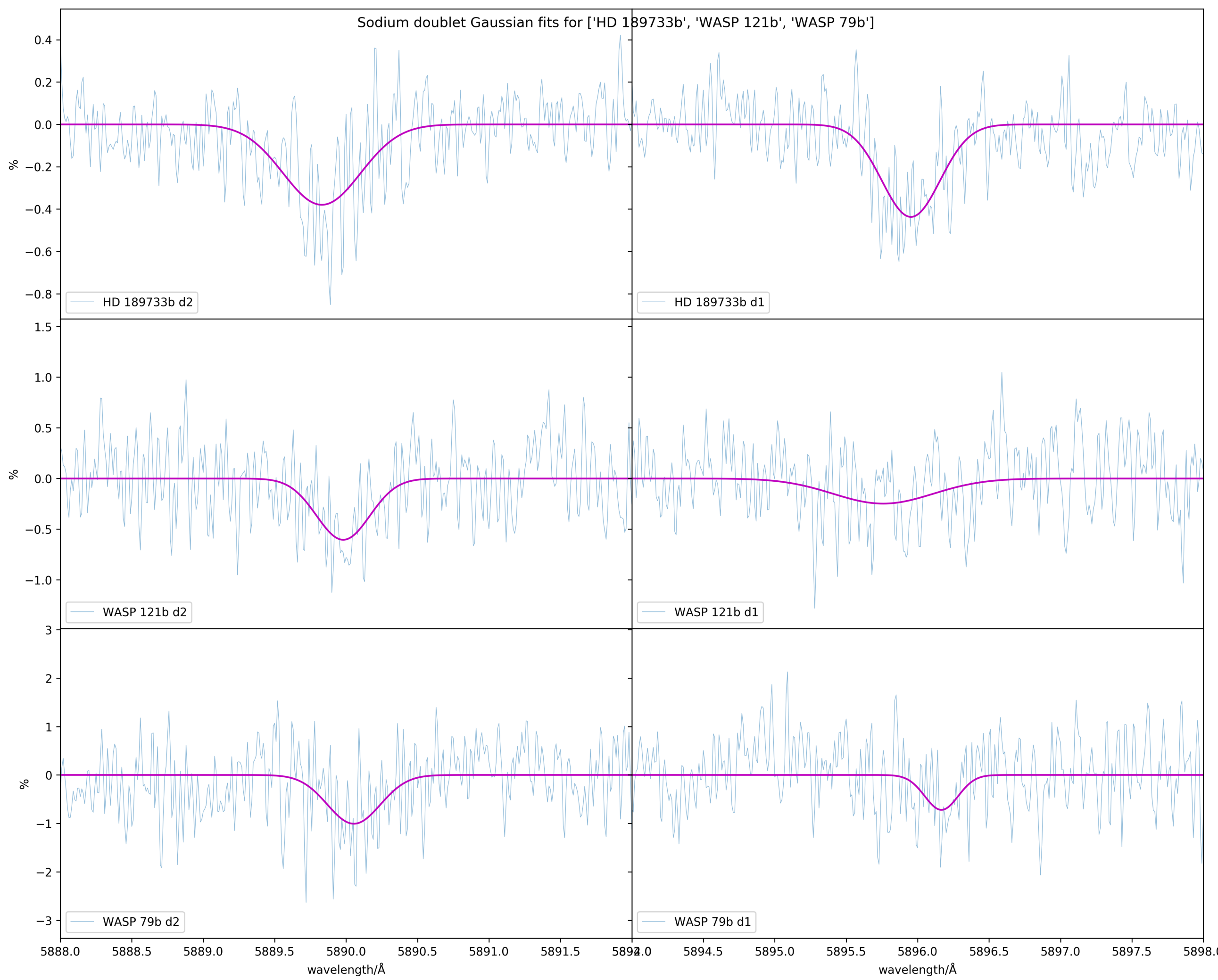

Figure 8: Gaussian fits to Na D2 and D1 lines in magenta. Original transmission spectra are in light blue.

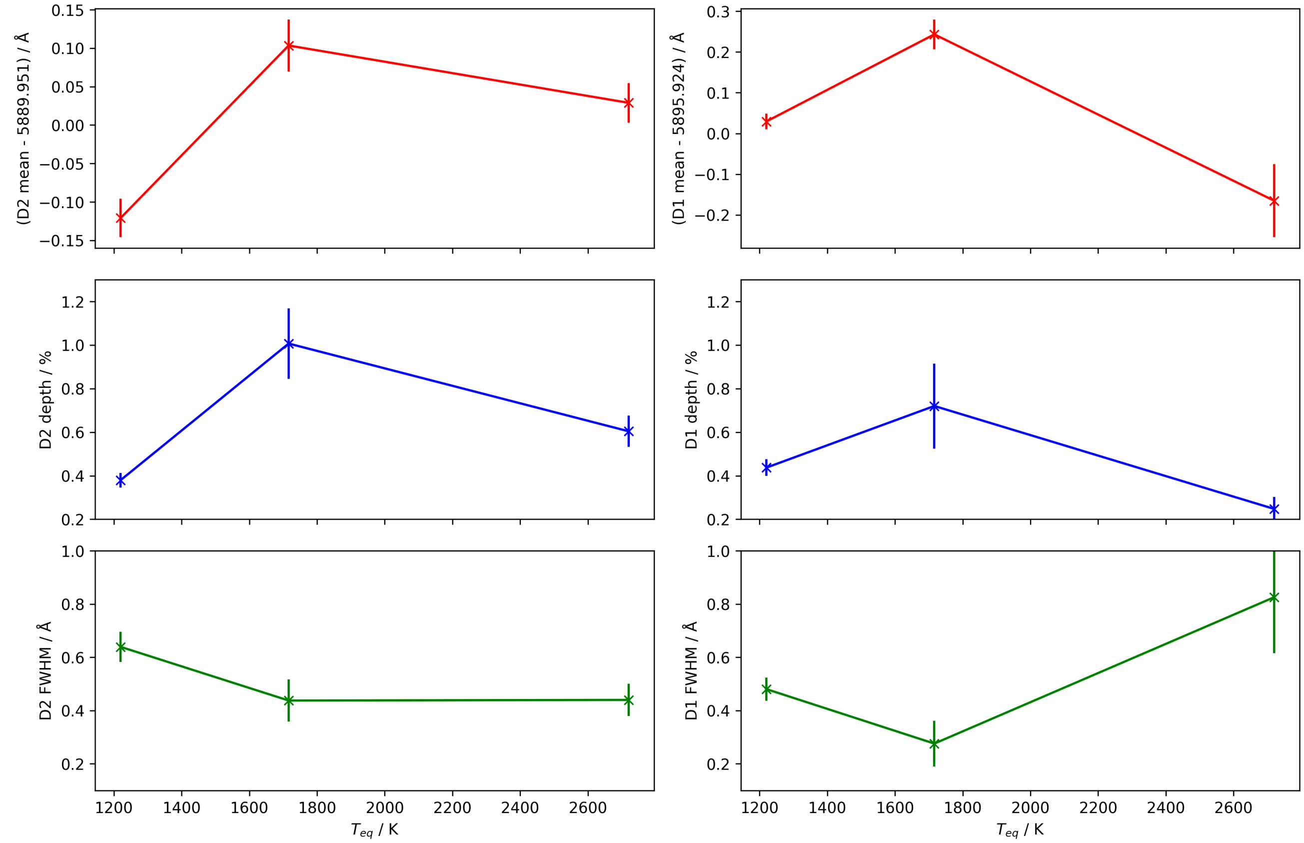

Figure 9: Gaussian fit results (mean, depth, FWHM) for D2 and D1 lines plot against equilibrium planetary temperature.

For WASP 121b, Cabot et al. 2020 reports 5890.01 ± 0.06 Å, -0.69 ± 0.12 % and 0.73 ± 0.09 Å for the D2 line, and 5896.09 ± 0.09 Å, -0.25 ± 0.09 % and 0.9 ± 0.1 Å for the D1 line. Sindel 2018 reports 5890.76 ± 0.04 Å, -0.495 ± 0.103 % and 0.37 ± 0.09 Å for the D2 line, and 5896.45 ± 0.16 Å, -0.179 ± 0.068 % and 0.84 ± 0.37 Å for the D1 line. A. Langeveld, Madhusudhan, and Cabot 2022 reports line depths of -0.65 ± 0.10 % (D2) and -0.37 ± 0.09 % (D1). These values indicate good agreement for both D2 and D1 parameters obtained in this work and confirm that the difficulties in clearly resolving the doublet for WASP 121b are not unique to this work.

3.3 Detection robustness analysis

3.3.1 Empirical Monte Carlo

To ensure the detections of sodium are statistically robust, we perform an empirical Monte Carlo (EMC) procedure. This is particularly important since there are a number of potential sources of systematic error, both from within the observations themselves and the data reduction process. For the former, for example, errors can arise from stellar variability and changing starspot distribution (Redfield et al. 2008) as well as the fact that the observations are spread out over many months. For the latter, within the pipeline we may introduce aberrations through the telluric corrections, continuum normalisation and stellar line subtraction. The EMC analysis applies bootstrapping to simulate alternate realisations of the data to consider whether the signal is genuine or transient, without requiring explicit modelling of the known and unknown sources of systematic error.

To perform the analysis, we first examine the dataset for a given target to determine the total number of in-transit observations, $N_{\rm in}$, and the total number of out-of-transit observations, $N_{\rm out}$. We once again ignore spectra which are on the boundary of the transit i.e. ingress and egress observations. Three different scenarios are constructed. The first is an "out-out" comparison, where we randomly select $N_{\rm in}$ spectra from the set of out-of-transit spectra, treat this as our "in-transit" observations set, and perform a transmission spectrum extraction against the full out-of-transit set of observations. The second scenario is an "in-in" comparison, where we instead randomly select $\sim N_{\rm in/N_{out}}$ spectra from the set of in-transit observations, treat this as our "in-transit" observations set, and perform a transmission spectrum extraction against the full in-transit set of observations (i.e. our "out-of-transit" set). The final scenario is an "in-out" comparison, where we randomly select $N_{\rm in}/2 \leq N \leq N_{\rm in}$ spectra from the in-transit observation set and perform a transmission spectrum extraction against the full out-of-transit set of observations. For all random selections we allow duplicate selection. We measure the absorption depth for each spectrum by measuring the mean flux over two 3 Å wide passbands centred on the D2 and D1 lines and subtracting the continuum level (estimated by averaging the mean flux over 5874.89 Å to 5886.89 Å (blue) and 5898.89 Å to 5910.89 Å (red)). Histograms of the absorption depth distributions for the three scenarios (each sampled ~ 2000 times) are presented in Figure 10.

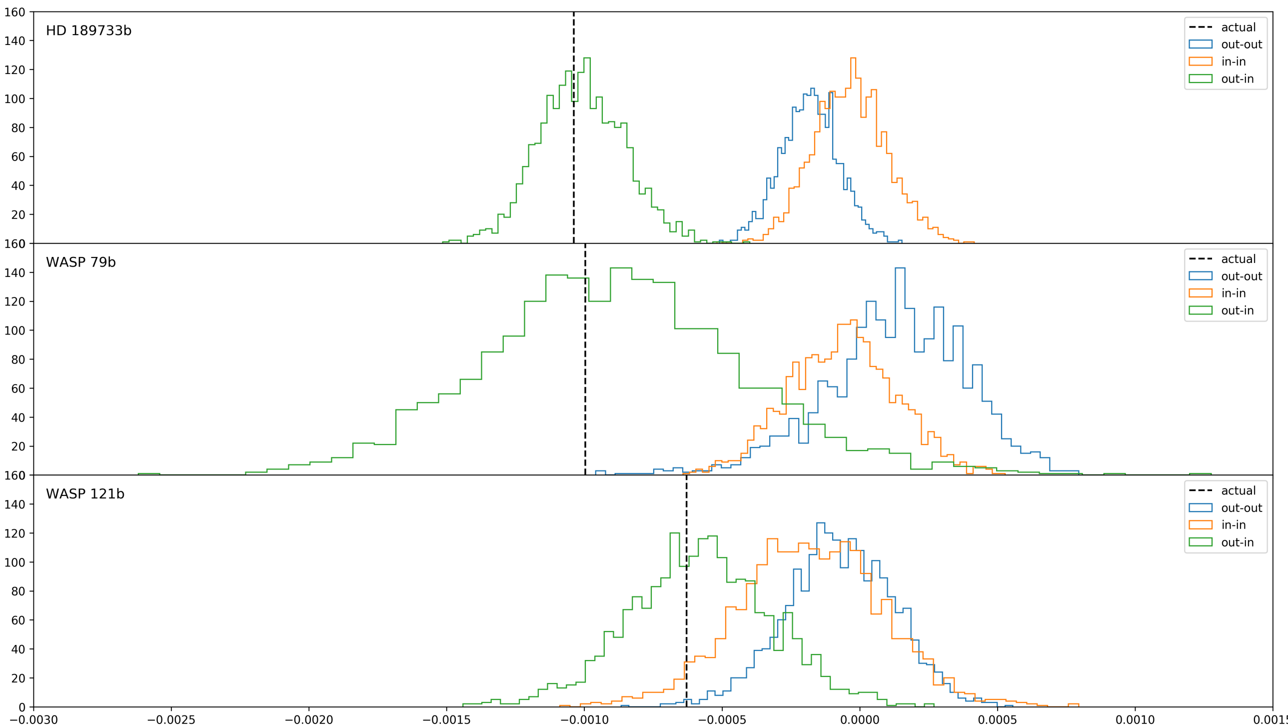

Figure 10: Empirical Monte Carlo results. The vertical black dashed line corresponds to the absorption depth measured for corresponding full spectrum.

In theory for a genuine sodium detection only the "in-out" scenario should have an absorption depth signal on average. We see that this is indeed the case for the three targets; the "in-in" and "out-out" histograms are all approximately centred on zero: for "in-in" we measure $\mu \pm \sigma$ (μ is distribution mean, σ is standard deviation) of -0.003 ± 0.013 (HD 189733b), -0.006 ± 0.019 (WASP 79b), -0.018 ± 0.026 (WASP 121b); for "out-out" we measure -0.018 ± 0.011 (HD 189733b), $+0.013 \pm 0.026$ (WASP 79b), -0.007 ± 0.020 (WASP 121b). The "in-out" distributions means are in agreement with the corresponding absorption depths in the full spectrum, which further confirms the validity of the detections: for "out-in" we measure -0.101 ± 0.015 (HD 189733b), -0.09 ± 0.05 (WASP 79b), -0.058 ± 0.026 (WASP 121b); for the full spectra absorption depths we measure -0.104 ± 0.012 (HD 189733b), -0.10 ± 0.06 (WASP

79b), -0.063 ± 0.032 (WASP 121b). The widths of the "out-out" distributions model the overall random and systematic noise associated with each detection (Redfield et al. 2008), so we quote our detection significance levels relative to these. **We conclude that we successfully detect sodium in the atmospheres of HD 189733b, WASP 79b and WASP 121b at 6.7σ, 3.9σ, and 4.1σ significance levels**.

3.3.2 Gaussian fit robustness

Having confirmed and better characterised the statistical significance of the sodium detections, we now consider the robustness of the Gaussian line profile fits to the data. The Levenberg-Marquardt algorithm used is quite sensitive to the initial parameter estimates provided to initialise the fitting procedure, so the optimisation could become stuck in local minima and not find the desired global minimum in the parameter loss landscape. To ensure we are achieving the true best fit to the data, we discretise the initial parameter estimate space and run the fitting algorithm at each point. We chose to scan the mean across 5887.0 Å to 5899.0 Å, the depth across -0.6 to 0.2 %, and the width across 0.2 Å to 0.9 Å. We chose to fit over a slice over a 100 Å of the data centred on the sodium doublet: while this does not make practical sense since we are fitting a single Gaussian to two features, in practice this does not affect the actual fitting parameters. Figure 11 shows resulting histograms over the three-dimensional output parameter space.

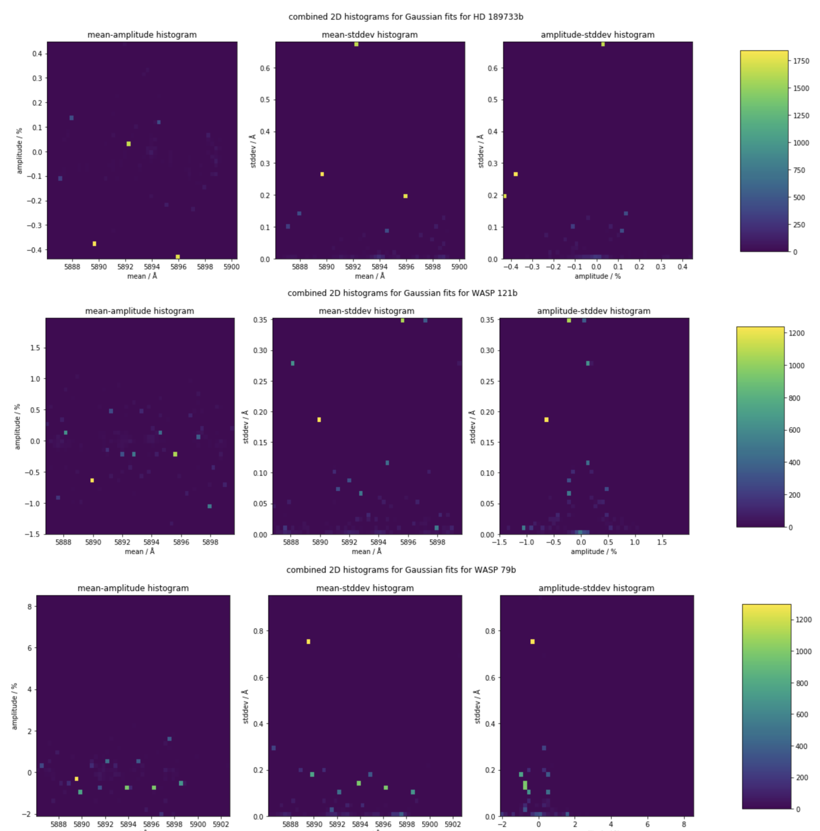

Figure 11: 3D histograms showing robustness of Gaussian fits to initial estimates. For each spectrum, we perform a grid search over initial estimates for line depth, position and FWHM and plot the density of the best fit result in 3D space.

For HD 189733b and WASP 121b there are two clear, well-defined peaks in the histograms corresponding to the D2 and D1 lines, thus indicating the fit results are robust to the initial parameter estimates. For WASP 79b there appears to be some degeneracy in the D2 line, but examining the most probable alternatives in Table 12, we can ignore the non-highlighted parameters on physical grounds.

	count	amplitude	mean	stddev
5	1299.0	-0.003472	5889.491022	0.758699
6	982.0	-0.006662	5893.830598	0.147922
4	958.0	-0.007726	5896.167293	0.119292
1	771.0	-0.009853	5889.991742	0.186096
8	679.0	-0.004535	5898.503988	0.100205
2	470.0	0.006099	5892.328437	0.100205
9	363.0	0.015670	5897.669454	0.014315
3	351.0	0.006099	5894.998946	0.186096
7	314.0	-0.006662	5891.660810	0.033402
0	253.0	0.002909	5886.653607	0.291073

Figure 12: Table showing possible degeneracy of Gaussian fits for WASP 79b.

4 Derived atmospheric properties

Having individually resolved and verified the Na D2 and D1 features for HD 189733b, WASP 121b and WASP 79b, we now make a series of inferences to characterise the atmospheric properties and processes of each target. This allows us to explore trends with atmospheric parameters across the three targets. We first consider the implied extent of sodium in the atmospheres from the line depths in subsection 4.1. We interpret our measured line profile shapes using the theory outlined in Heng et al. 2015 in subsection 4.2 to measure potential temperature gradients.

4.1 Atmospheric extent of sodium

The first set of inferences we can make pertain to the extent of sodium present in the atmospheres through the average line depths. We recall that for in-transit spectra, we define the continuum flux value as the white-light transit depth Δ_0 which corresponds to the decrease in flux received due to the planet's transit. This is equal to the ratio of the sky-projected areas of the planet and the star:

$$\Delta_0 = \frac{\pi R_p^2}{\pi R_s^2} = \left(\frac{R_p}{R_s}\right)^2. \tag{3}$$

For a species with strong absorption at a given wavelength λ we expect to see an excess transit depth δ_λ relative to the continuum transit depth due to the additional area blocking the stellar flux. If we take the maximum height (above the white light radius) up to which the absorbing species is present as H_λ, we can approximately relate δ_λ to H_λ:

$$\delta_\lambda = \frac{\pi(R_p + H_\lambda)^2}{\pi R_s^2} - \Delta_0 \approx \frac{R_p^2 + 2R_p H_\lambda}{R_s^2} - \frac{R_p^2}{R_s^2} = \frac{2\Delta_0 H_\lambda}{R_p} \tag{4}$$

This expression makes the empirically motivated assumption that $H_\lambda \ll R_s^2$. For consistency across targets, we express H_λ in atmospheric scale heights $H_{\rm sc}$, which are defined as the increase in altitude over which the pressure decreases by a factor of e:

$$H_{\rm sc} = \frac{k_B T_{\rm eq}}{\mu_m g} \tag{5}$$

where k_B is the Boltzmann constant, $T_{\rm eq}$ is the equilibrium temperature, μ_m is the mean molecular weight, and g is the planet's surface gravity (assuming minimal variation of g with altitude). We assume a $\mu_m = 2.22$u to match Jupiter.

The average sodium line depths of 0.4044±0.0006 %, 0.890±0.015 %, and 0.3783±0.0019 % correspond to $33.49 \pm 0.05H_{\rm sc}$, $55 \pm 1H_{\rm sc}$, and $14.54 \pm 0.07H_{\rm sc}$. As per Madhusudhan 2019 "a saturated spectral feature in a a transmission spectrum is expected to to have an amplitude of 5-10 scale heights". This suggests our Na detections must probe the upper regions of their respective atmospheres.

4.2 Non-isothermal behaviour

Given this, we can further investigate the characteristics of the Na detections to probe for evidence of behaviour beyond our current tacit assumptions of isothermal temperature profiles and hydrostatic equilibrium. We first tackle evidence for non-isothermality by constructing a zeroth order estimate for the temperature within the region of the atmosphere probed by the Na detection. By enforcing a depth of 5 to 10 scale heights for the average feature, we can invert equation 5 to infer temperature ranges of $T \sim 4085 - 8170$K, $9522 - 19045$K, and $3954 - 7908$K for the thermospheres.

We can obtain deeper insights by adopting a more rigorous approach to non-isothermality as outlined in Heng et al. 2015, which illustrates how we can infer the presence of a temperature gradient through considering the absorption depths and transit radii for a feature. Consider a linear series expansion of the temperature i.e. $T = T_{\rm ref} + \frac{\partial T}{\partial z} z$ where $T_{\rm ref}$ is a reference temperature. We take the gradient as a constant (either positive or negative) and denote it as $\frac{\partial T}{\partial z} = \pm T'$ where T' is positive. Hydrostatic equilibrium is also assumed i.e. $\frac{\partial P}{\partial z} = -\rho g$ where P is the pressure, ρ the mass density of the atmosphere and g the gravitational acceleration (taken as constant). From the ideal gas law $P = nk_BT$ we obtain (Heng et al. 2015):

$$\ln(n/n_{\rm ref}) = -\frac{\mu_m \tilde{g}}{k_B} \int_0^z \frac{1}{T_{\rm ref} \pm T'z} dz \implies n = \begin{cases} n_{\rm ref} \left(1 + \frac{T'z}{T_{\rm ref}}\right)^{-(b+1)}, & \frac{\partial T}{\partial z} > 0 \\ n_{\rm ref} \left(1 - \frac{T'z}{T_{\rm ref}}\right)^{b-1}, & \frac{\partial T}{\partial z} < 0 \end{cases} \tag{6}$$

where we define $\tilde{g} = g \pm k_BT'/m$ as an effective gravity and the index b is the ratio of non-isothermal scale height to isothermal scale height:

$$b = \frac{T_{\rm ref}/T'}{k_b T_{\rm ref}/\mu_m g} = \frac{\mu_m g}{k_b T'}. \tag{7}$$

We assume a Doppler line profile at the line centre. Omitting the details of the derivation for brevity, we can derive an expression for the number density at line centre n_0:

$$n_0 = \ln\left(\frac{F_0}{F_c}\right) \frac{m_e c}{\xi \pi e^2 f_{\rm lu} \lambda_0} \left(\frac{k_B T'}{\pi \mu_m R_0}\right)^{1/2} \tag{8}$$

where (F_0/F_c) is the ratio of fluxes measured at line centre and for the continuum, ξ is an order unity constant, m_e and e the mass and charge of the electron, $f_{\rm lu}$ the sodium oscillator strength, R_0 and λ_0 the radius and wavelength at the line centre.

At line wings we assume a Lorentzian profile on empirical grounds. This allows us to generate a further expression for the number density n and thus eliminate to solve for T. In the isothermal case, we have (Heng et al. 2015):

$$T = \frac{mg\Delta R}{k_B \ln r} \tag{9}$$

where

$$r \approx (6 \times 10^3) \frac{\ln(F/F_c)}{\ln(F_0/F_c)} \left(\frac{R_0}{R}\right)^{1/2} \left(\frac{T}{10^3 K}\right)^{-1/2} \left(\frac{\mu_m}{2m_H}\right)^{1/2} \left(\frac{\Delta\lambda}{0.1\mathring{A}}\right)^2, \tag{10}$$

quantity	HD 189733b		WASP 79b		WASP 121b	
observables	centre	wing	centre	wing	centre	wing
D2 $(1 - F_\lambda/F_c), \%$	0.3798	0.2062	1.0067	0.2733	0.6041	0.1663
D1 $(1 - F_\lambda/F_c), \%$	0.4370	0.1483	0.7201	0.0271	0.2475	0.0271
D2 R_λ, $\mathrm{R_J}$	1.225	1.186	2.287	1.858	2.071	1.846
D1 R_λ, $\mathrm{R_J}$	1.238	1.173	2.129	1.690	1.890	1.849
analysis						
$\Delta R_1/\Delta R_2$	1.66		1.03		0.18	
+ or − gradient	−		−		−	
results						
T_{thermo}, K	$\sim 4085 - 8170$		$\sim 9522 - 19045$		$\sim 3954 - 7098$	
T_1, K	2772		10422		689.7	
T_2, K	1543		7697		4573	
$\partial T/\partial z$, $\mathrm{Kkm^{-1}}$	-1.324		-0.2316		-19.06	

Table 3: Summary of non-isothermal theory observables, analysis and results.

$\Delta R = R_0 - R_\lambda$, and $\Delta\lambda = \lambda - \lambda_0$. For the non-isothermal case we instead have (Heng et al. 2015):

$$T = \begin{cases} T'\Delta R[r^{1/(b+1)} - 1]^{-1}, & \frac{\partial T}{\partial z} > 0 \\ T'\Delta R[1 - r^{-1/(b-1)}]^{-1}, & \frac{\partial T}{\partial z} < 0 \end{cases}. \tag{11}$$

where b is the same index as above.

How do we operationalise the equations above to estimate the temperature gradient for a given target? We first collect our observables from the Gaussian fits: the absorption depth F_λ/F_c and effective radius R_λ, measured at the line centres and at the line wings (approximated as $\Delta\lambda = 0.3\,\text{Å}$ from the centres) for both D2 and D1 lines. Note that we can relate the absorption depth and effective radius by simple manipulation of equation 4. We then determine the whether the atmosphere shows evidence of non-isothermality by checking the ratio $\Delta R_1/\Delta R_2$, where ΔR_1 and ΔR_2 correspond to the difference in radius (ΔR) at the centre and at the wing the D1 and D2 features respectively. From equation 9 this ratio should be ~ 1 for an isothermal system; if this is the case then we calculate T directly from equation 9. For the non-isothermal case, we then generate isothermal estimates for T_1 and T_2 (the temperatures probed by the D1 and D2 features respectively) from equation 9: we take initial estimate $T = 1000\,\text{K}$, calculate r, and update T iteratively until convergence. This allows us to check the sign of $\frac{\partial T}{\partial z}$ using the ratio $\frac{\partial T}{\partial z} = \frac{T_1 - T_2}{R_1 - R_2}$. Having determined this, we apply the relevant case in equation 11 to iterate for T_1, T_2 and T' as required. The results from this procedure are summarised in Table 3 and discussed further in section 5.

4.3 Non-hydrostatic exosphere

We now turn to consider evidence the assumption thus far of hydrostatic equilibrium. Hydrostatic equilibrium is known to be an excellent approximation in the dense troposphere, but given our detections probe the upper atmosphere we can anticipate this approximation may not continue to hold, especially within the exosphere where the atmosphere transitions from a collisional to collisionless fluid. This hydrostatic disequilibrium can manifest itself through different evaporative models including spherical atmospheric escape, a spherical cloud sourced by an outgassing satellite (e.g. exomoon), and a toroidal cloud sourced by a satellite or debris. These scenarios introduce number density profiles $n(r, \phi, \theta)$ for Na which are materially different to the hydrostatic profile given by $n_{\rm hyd}(r) = n_0 \exp(\lambda(r) - \lambda_0)$, where $\lambda(r) = \frac{GM_p\mu_m}{rk_BT}$ is the Jeans parameter. As the number density profile $n(r, \phi, \theta)$ directly influences the characteristics of the sodium doublet in transmission spectra, it is possible through inverse modelling to constrain the presence and nature of a possible atmospheric hydrostatic disequilibrium.

Gebek and Oza 2020 undertakes the forward modelling of these different evaporative scenarios and proposes a diagnostic, the Na D2/D1 absorption depth ratio $f_{D2/D1}$, which can partially constrain the possible evaporative processes present from observations. The D2/D1 absorption depth ratio $f_{D2/D1}$ is calculated by integrating the transmission spectrum over small passbands (chosen here to be width 1.5 Å) centred on the D2 and D1 features, and taking the ratio of these absorption depths:

$$f_{D2}/f_{D1} = \frac{\int_{\lambda_{\rm D2}-1.5/2}^{\lambda_{\rm D2}+1.5/2}(1 - F_\lambda/F_c)\ d\lambda}{\int_{\lambda_{\rm D1}-1.5/2}^{\lambda_{\rm D1}+1.5/2}(1 - F_\lambda/F_c)\ d\lambda}. \tag{12}$$

This diagnostic also physically corresponds to a signal for the optical thickness of the regime where the majority of absorption is taking place: a $f_{D2/D1} \gtrsim 2$ indicates absorption predominantly occurs in the optically thin regime, while $f_{D2/D1} \lesssim 1$ indicates majority absorption in the optically thick regime. The Gebek and Oza 2020 work considers three forward modelling cases. The first is the control: a hydrostatic atmosphere with no significant heating i.e. $T = T_{\rm eq}$. The results indicate this corresponds to a $f_{D2/D1} \approx 1$ with absorption predominantly occurring in a single small but very optically thick layer. The second case is a hydrostatic atmosphere with significant thermospheric heating i.e. $T = 10 \times T_{\rm eq}$. Here the atmosphere is more puffed up, stretching the size of the optically thick layer compared to the control; this overall results in an slightly increased $f_{D2/D1} \approx 1.1$. The third case is that of a non-hydrostatic evaporative atmosphere (either spherical, exomoon or toroidal). Due to the longer tail of the number density profile $n(r, \phi, \theta)$, the absorption is seen to predominantly occur in the optically thin regime which corresponds to $f_{D2/D1} \approx 2$. This means if we observe $f_{D2/D1} \gtrsim 1.2$, it is unlikely that the absorption is occurring in the optically thick regime, meaning we can rule out hydrostatic equilibrium even with significant thermospheric heating.

We obtain $f_{D2/D1} = 1.13 \pm 0.24, 1.6 \pm 1.2, 1.4 \pm 0.6$. For HD 189733b this is inconclusive: a value of 1.13 ± 0.24 is consistent with both hydrostatic and evaporative scenarios. WASP 79b and WASP 121b both suggest evaporative exospheres, but may prove to be beyond the scope of the forward modelling results since they both probe the upper ends of the temperature scale for hot Jupiters at $T_{\rm eq} = 1716$ K and 2720 K respectively (which were not considered in the Gebek and Oza 2020 work). These results are discussed further in section 5.

4.4 Atmospheric dynamics

Focusing on the positions and widths of the sodium features, we can also constrain the atmospheric dynamics for the exoplanets considered. Within the lab rest frame, the sodium D2 and D1 line are measured to be 5889.951 Å and 5895.924 Å respectively. Spectral lines from atmospheric sources typically have widths dominated by thermal Doppler broadening given by:

$$\Delta\lambda_{\rm FWHM} = \left(\frac{8k_BT\ln 2}{mc^2}\right)^{1/2} \lambda_0 \tag{13}$$

where T and m are the temperature and atomic mass of the absorbing species, and λ_0 the spectra line wavelength in the lab rest frame. Taking $T = T_{\rm eq}$ and convolving with the HARPS instrument line spread function (typically represented by a Gaussian with width 0.05 Å (Wyttenbach et al. 2015)) we get an expected FWHM of ~ 0.06 Å for the three targets. Referring back to Table 2, it is clear that both lines are shifted and broadened for all targets. We can reconcile these observation by considering the effects of atmospheric dynamics, specifically two types of winds: day-to-nightside winds and zonal jet streams.

We motivate the presence of the former by the fact that hot-Jupiters are expected to be tidally locked resulting in permanent day and night sides. The stellar irradiation builds up on a "hot spot" on the dayside which then triggers winds of order $\sim 1-10$ km/s due to the temperature contrast ΔT, typically spanning the 10^{-3} bar pressure regime. The primary effect of this day-to-nightside wind on the sodium features is to introduce a Doppler shift due to the relative motion in the line of sight of the observer; we can thus deduce the wind speed through the following equation:

$$v_{\text{wind}} = c\left(\frac{\lambda_{\text{obs}}^2 - \lambda_{\text{lab}}^2}{\lambda_{\text{obs}}^2 + \lambda_{\text{lab}}^2}\right) \tag{14}$$

where λ_{obs} is the feature peak wavelength and λ_{lab} the corresponding lab rest frame wavelength. We can relate v_{wind} to the day-night temperature contrast ΔT by considering the longitudinal force balance at the equator: we can equate the convective acceleration $\vec{v} \cdot \vec{\nabla}\vec{v} \sim v_{\text{wind}}^2/R_p$ to the temperature-pressure gradient $\sim \mathcal{R}\Delta T \Delta \ln p/R_p$, where $\mathcal{R}$ is the gas constant and we assume the wind vertically extends over a range $\Delta \ln p \approx 3$. This leads to equation 15 (A. P. Showman, Cho, and Menou 2010).

$$v_{\text{wind}} \sim (\mathcal{R}\Delta T \Delta \ln p)^{1/2} \tag{15}$$

Zonal jet streams (concentrated on the equator) are also likely to be present on hot-Jupiters based on results in the literature exploring 3D atmospheric dynamics modelling (e.g. Flowers et al. 2019; Steinrueck et al. 2019; Debrecht et al. 2019) and are expected to span the 1 bar pressure regime. These winds rotate into the direction of planetary rotation meaning the net effect is a super-rotation of the atmosphere i.e. $v_{\text{total}} = v_{\text{jet}} + v_{\text{rotation}}$. This introduces a rotational broadening of the spectral features: since different fluid elements are Doppler shifted by different amounts, the overall composition of the signals is broader than the width of each individual signal.

Typically the quantitative implications of this phenomenon are calculated through forward modelling: approximating the atmosphere as a flat annulus and mapping it onto a grid, each grid pixel is assigned a synthetic unbroadened sodium absorption profile which is Doppler shifted by the atmospheric wind at that pixel. The sum of the profiles at the observer produces an overall observed spectral feature; using inverse modelling this can be fit to an observed profile to deduce v_{total}. We opt to neglect this detailed approach within this work and instead attempt to generate estimates for v_{total} for our targets by linearly extrapolating the results of Keles 2021, which performs an inverse modelling analysis for 7 planets. Figure 13 shows the data and results for this regression; the approximate relationship for the D2 line is:

$$v_{\text{total}} = \left[(33 \pm 7)\left(\frac{\Delta\lambda_{\text{rot}}}{1\,\text{Å}}\right) + (-4 \pm 3)\right]\,\text{km}\,\text{s}^{-1}. \tag{16}$$

By measuring the difference in FWHM between theory and observation and equating this to the rotational broadening FWHM, $\Delta\lambda_{\text{rot}} = \sqrt{\Delta\lambda_{\text{obs}}^2 - \Delta\lambda_{\text{theory}}^2}$, we can estimate v_{total}, which in term allows us to estimate v_{jet} by assuming perfect tidal locking i.e. $v_{\text{rotation}} = 2\pi R_p/P$ (where P is the orbital period obtained from the NASA Exoplanet Archive). The results for these procedures are summarised in Table 4 and discussed further in section 5.

4.5 Clouds and hazes

Finally we consider possible evidence for the presence of cloud/hazes within the atmospheres of our targets. Following the analysis of Heng 2016, a cloud-free atmosphere should have a well defined difference between

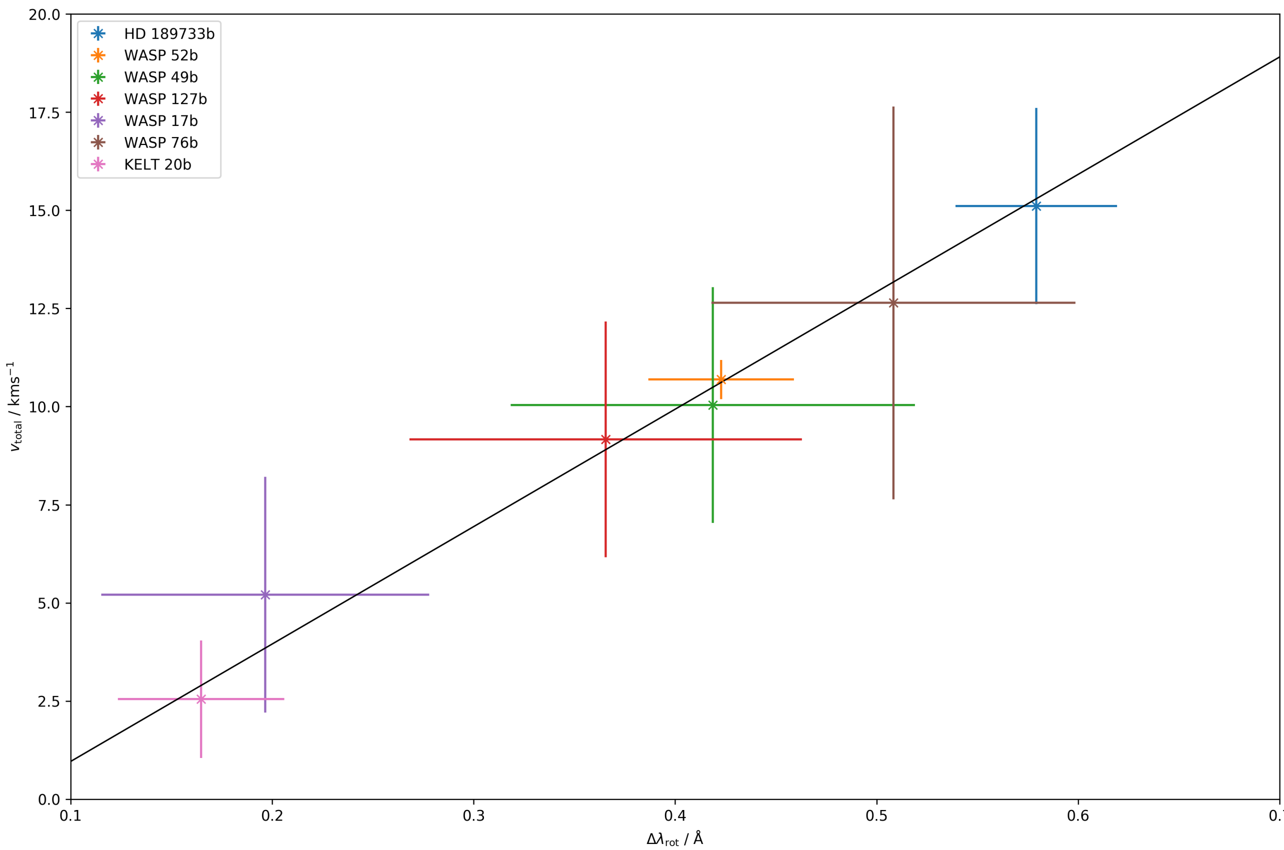

Figure 13: Plot showing velocity data from Keles 2021 from inverse modelling against corresponding observed rotational broadening width. The black line represents the linear fit to the data used to extrapolate the results to the observed rotational broadening widths measured in this work.

quantity	HD 189733b		WASP 79b		WASP 121b	
theoretical	D2	D1	D2	D1	D2	D1
$\Delta\lambda_{\text{theory}}$, Å	0.0587	0.0587	0.0619	0.0619	0.0678	0.0679
observables	D2	D1	D2	D1	D2	D1
$\lambda_{\text{obs}} - \lambda_{\text{lab}}$, Å	-0.121 ± 0.025	0.029 ± 0.019	0.10 ± 0.03	0.24 ± 0.04	0.029 ± 0.026	-0.16 ± 0.09
$\Delta\lambda_{\text{obs}}$, Å	0.64 ± 0.06	0.48 ± 0.04	0.44 ± 0.08	0.28 ± 0.09	0.44 ± 0.06	0.83 ± 0.21
$\Delta\lambda_{\text{rot}}$, Å	0.64 ± 0.06	0.48 ± 0.04	0.43 ± 0.08	0.27 ± 0.09	0.43 ± 0.06	0.82 ± 0.21
results						
v_{wind}, km s^{-1}	-1.4 ± 0.6		8.6 ± 1.6		0.7 ± 1.6	
v_{total}, km s^{-1}	17 ± 5		11 ± 5		11 ± 4	
v_{jet}, km s^{-1}	14 ± 5		9 ± 5		4 ± 4	

Table 4: Summary of atmospheric dynamics observables, analysis and results.

the the transit radii at line centre and wing, $\Delta R = R_0 - R_\lambda$. Assuming an approximately isothermal atmosphere and Lorentzian profile at line wings we find:

$$\Delta R_{\text{theory}} = H_{sc} \ln \left[\lambda_0 \Phi^{-1} (2\pi H g)^{-1/2} \right] \tag{17}$$

variable	symbol	unit	HD 189733b	WASP 79b	WASP 121b
scale height	H_{sc}	-	33.49 ± 0.05	55 ± 1	14.54 ± 0.07
thermosphere temperature	T_{thermo}	K	$\sim 4085 - 8170$	$9522 - 19045$	$3954 - 7908$
temperature at Na D1 line	T_1	K	2772	10422	689.7
temperature at Na D2 line	T_2	K	1543	7697	4573
temperature gradient	$\partial T/\partial z$	$\mathrm{K km^{-1}}$	-1.324	-0.2316	-19.06
D2-D1 absorption depth ratio	$f_{D2/D1}$	-	1.13 ± 0.24	1.6 ± 1.2	1.4 ± 0.6
day-to-nightside wind speed	v_{wind}	$\mathrm{km\,s^{-1}}$	-1.4 ± 0.6	8.6 ± 1.6	0.7 ± 1.6
day-to-nightside temperature contrast	ΔT	K	160 ± 150	6500 ± 2400	45 ± 203
total rotational wind speed	v_{total}	$\mathrm{km\,s^{-1}}$	17 ± 5	11 ± 5	11 ± 4
zonal jet stream wind speed	v_{jet}	$\mathrm{km\,s^{-1}}$	14 ± 5	9 ± 5	4 ± 4
D1 cloudiness index	C_{D1}	-	3.3	2.0	27
D2 cloudiness index	C_{D2}	-	5.4	2.0	4.9

Table 5: Summary of atmospheric inferences made for three targets.

where H_{sc} is the scale height as defined in 5, λ_0 the wavelength at line core, g the surface gravity and Φ the Lorentz profile given by equation 18.

$$\Phi = \frac{A_{21}\lambda^2\lambda_0^2}{4\pi^2 c^2(\lambda - \lambda_0)^2} \tag{18}$$

We assume $\mu_m = 2.22$, $T = T_{eq}$, take the Einstein A-coefficient $A_{21} = 6.137 \times 10^7\,\mathrm{s^{-1}}, 6.159 \times 10^7\,\mathrm{s^{-1}}$ for the D1 and D2 Na lines, $\Delta\lambda = 0.3\,\text{Å}$, and neglect pressure broadening since this is only important at $p \gtrsim 1\,\text{bar}$ (Allard et al. 2012) as before.

A cloudy/hazy atmosphere by contrast should have a lower value of ΔR due to the cloud/haze increasing the continuum transit radius (as more stellar flux is blocked) thus dimming the spectral features. As such we can define a dimensionless cloudiness index $C = \Delta R_{\text{theory}}/\Delta R_{\text{obs}}$; a value $C \approx 1$ corresponds to a perfectly cloud free atmosphere, whereas a value $C \gg 1$ suggests the presence of clouds or hazes. We find for our targets $C_{\text{D2}} \approx 5.4, 2.0, 4.9$ and $C_{\text{D1}} \approx 3.3, 2.0, 27$.

4.6 Trends with atmospheric properties

We summarise the results of the above analysis in Table 5 below.

Taking a different approach, we now directly examine the dataset for trends to identify relationships between the sodium features and atmospheric parameters. This endeavour is limited by the fact that we only have a sample size of three, but can nonetheless provide a starting point for further, more comprehensive study. We partition the data into two disjoint sets: the predictors (i.e the independent variables) and the predictands (i.e. the dependent variables which have been measured through spectral observations). The predictors include: the planetary equilibrium temperature T_{eq}, the stellar effective temperature T_s, the planetary surface gravity g_p, the planetary density ρ, the total incident stellar flux F_s, the escape velocity $v_{\text{esc}} = \sqrt{2GM_p/R_p}$, and the Jeans parameter $\lambda_J \approx (GM_p\mu_m/R_p k_B T_{\text{eq}})$. The predictands include: the average (across D2 and D1) feature depth in scale heights, the average feature FWHM, the average Doppler shift, the estimated temperature gradient $\partial T/\partial z$, the D2/D1 absorption depth ratio $f_{\text{D2/D1}}$, v_{wind}, v_{jet}, and the cloudiness index for the D2 feature C_{D2}. Note we include the feature depth in scale heights instead of raw % for fair comparison across targets, and omit the C_{D1} data due to the anomalously high WASP 121b value.

We analyse each subset of the full dataset to check for internal correlations, before considering correlations between the predictors and predictand subsets. The results of this analysis are presented in Figure 14.

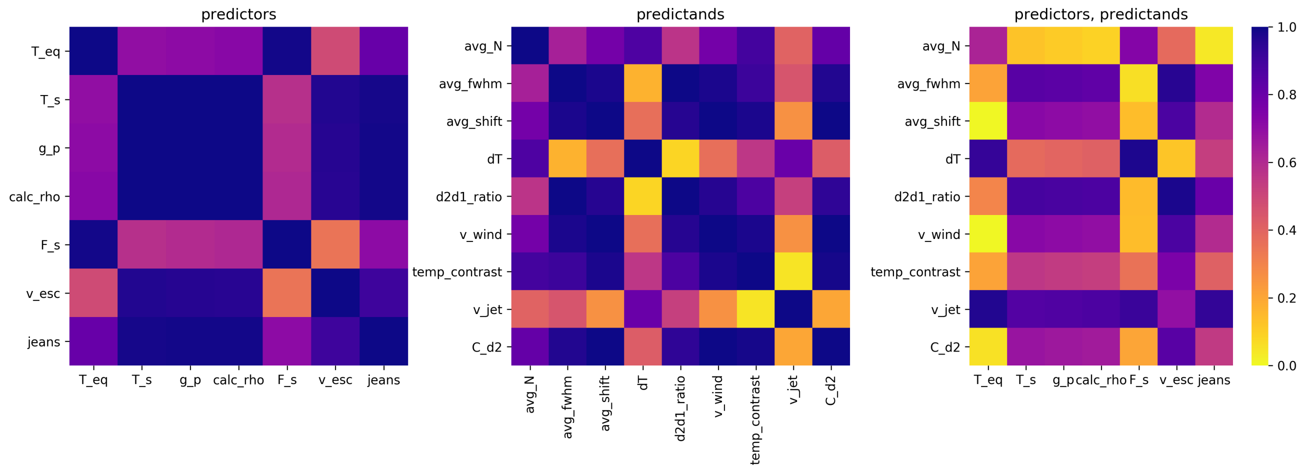

Figure 14: Heat maps showing absolute Pearson correlation coefficients for datasets.

5 Comparative analysis

The detections of sodium in the upper atmosphere have allowed us to make a number of inferences about the atmospheres for all three targets. We find strong evidence for non-isothermal temperature structure for all three targets, both through considering thermospheric heating and estimating the temperature gradient with altitude. WASP 79b appears to have the strongest thermospheric heating based on the estimates for T_{thermo}, T_1 and T_2. This could perhaps be explained by that fact that it has the highest stellar temperature $T_s = 6600\,\text{K}$. All targets appear to have a negative temperature gradient, which could be interpreted as evidence against thermospheric heating and thermal inversions. This is in tension with the estimates of T_{thermo}, T_1 and T_2 as well as current temperature profile modelling in the literature. For HD 189733b Huitson et al. 2012 conclude from Hubble Space Telescope (HST) observations that the temperature gradient should be positive, with Wyttenbach et al. 2015 estimating a value $\sim 0.2\,\text{Kkm}^{-1}$ but no thermal inversion. Mikal-Evans, Sing, Kataria, et al. 2020 find evidence also using HST observations for a positive temperature gradient, going so far as to suggest a thermal inversion. WASP 79b results appear inconclusive: Baxter et al. 2020 find infrared dayside emission spectra to be show limited evidence of thermal inversion. A possible reason for this lack of consistency in the results is that the method of Heng et al. 2015 applied relies greatly on accurate measurements of the line wings of the sodium features, which are difficult to extract from the optical observations using the methodology applied within this work, since a great deal of continuum signal (which may contain line wing data) is discarded in normalisation. Complementing the analysis within this work with low resolution space-based observations would help recover continuum information and allow for more rigorous inferences to made using inverse modelling.

All three targets show some evidence of an exosphere with evaporative processes through the measured D2/D1 ratios, particularly WASP 79b and WASP 121b. This is consistent with the literature: for HD 18973b Bourrier et al. 2013 reports atmospheric escape using HST observations of the H Lyman-α line; and for WASP 121b Sing et al. 2019 detect an exosphere using HST observations of Mg and Fe features, and D. Yan et al. 2021 estimate a mass loss rate of $\sim 1.28 \times 10^9\,\text{kg}\,\text{s}^{-1}$ from hydrodynamical simulations. Additionally, the Gebek and Oza 2020 work used for the analysis in this section of the project includes inverse modelling for a number of evaporative scenarios: they conclude that a toroidal envelope is consistent with the WASP 121b data.

We find good evidence for all targets of atmospheric winds, specifically day-to-nightside winds in the upper atmosphere and super-rotational zonal jets in the lower atmosphere. For WASP 79b, the day-to-night wind speed and corresponding temperature contrast are anomalously high, likely due to inaccurate measurement of the spectral feature Doppler shifts from to limited data. The magnitudes of the speeds are consistent with more detailed general circulation models for WASP 121b and HD 189733b, but further observations are required to reduce the size of the error bars - the current data quality only allows for broad estimation of the wind speeds. The zonal jet stream speeds are found to be consistent with more detailed modelling; we are able to replicate the trend observed by Keles 2021 of decreasing jet speed with temperature for our targets. A possible explanation for this is an atmospheric drag force induced by the ionisation of the alkali line at elevated atmospheric temperatures - observations in the UV to probe for these charged species could help confirm this in future work.

Considering the more speculative correlation analysis, we first note that the conclusions made here are all limited due to the small sample size considered - a larger study is required to check whether these relationships generalise to the population level. Examining the internal trends within the predictors and predictands sets to avoid identifying degenerate relationships. Within the predictors we find a number of strong correlations. T_{eq} and F_s are seen to be well correlated - this is unsurprising given $F_s \sim T_{\text{eq}}^4$ in theory. g_p, ρ, v_{esc} also show strong correlation; this is likely the result of the fact the targets mass and radii only vary from $0.850\,\mathrm{M_J}$ to $1.157\,\mathrm{M_J}$ and $1.138\,\mathrm{R_J}$ to $1.753\,\mathrm{R_J}$, since these parameters all scale with powers of M_p and R_p. The strong negative correlation between T_s and g_p indicates $T_s \sim M_p^{-1}R_p^2$; combined with the strong correlation with λ_J this indicates perhaps $a \sim M_p^{-2}R^7$.

Within the predictands, we first check the core observables: the depth, FWHM and Doppler shifts are not strongly correlated, which provides evidence they each carry causally independent information. Next, we examine the derived observables to check their relationships with the core observables. The temperature gradient correlates strongly with the average feature depth, suggesting the other core observable involved, the FWHM, has limited impact. The D2/D1 is also calculated from the depth and FWHM but exhibits an inverse relationship with FWHM - this is expected since we essentially divide out the dependence on the depth in calculating the ratio. As expected, the day-to-nightside wind speed is strongly positively correlated with the Doppler shift; more unusually it is also strongly correlated with the average feature depth and negatively correlated with the average FWHM. The zonal jet speed only presents a modest positive correlation with the average FWHM despite it being derived exclusively from this observable: this indicates atmospheric parameters (i.e. R_p and the orbital period P) dominate the calculation.

Turning to consider the predictors and predictands together, we identify a number of notable relationships which could be indicative of broader trends in the hot Jupiters. First, we see that the D2/D1 ratio is strongly negatively correlated with both the escape velocity and the Jeans parameter. This validates its designation as a diagnostic for a non-hydrostatic atmosphere since low values of the escape velocity and Jeans parameter indicate significant probability of atmospheric escape. Secondly, we observe positive correlation between the planetary surface gravity and the zonal jet speed. Since the zonal jets appear to originate from the interaction between atmospheric waves in the lower atmosphere and the planetary rotation, this could indicate the atmospheric waves are gravitational in nature. Thirdly, we see a positive correlation between the stellar temperature and the day-to-nightside wind. The lack of correlation with the equilibrium planetary temperature perhaps appears to confirm that these winds are confined to the upper atmosphere, where stellar irradiation may drive thermospheric heating. There is an empirical trend between the temperature of hot Jupiters and high day-to-nightside temperature contrast (Perez-Becker and Adam P. Showman 2013) - if the mechanism behind this scales with the stellar temperature instead the planetary equilibrium temperature, then this can explain the correlation between with the day-to-nightside wind. Finally, we observe a negative correlation between the stellar temperature and the cloudiness - a possible explanation is that the upper atmosphere again scales with the stellar temperature instead of the planetary equilibrium temperature, and a colder upper atmosphere induces the formation of condensates/clouds.

6 Conclusion

We performed a homogeneous analysis to detect atmospheric sodium using high-resolution transmission spectroscopy for a sample of three planets spanning the hot Jupiter regime: HD 189733b ($T_{eq} = 1220\,\mathrm{K}$), WASP 79b ($T_{eq} = 1716\,\mathrm{K}$) and WASP 121b ($T_{eq} = 2720\,\mathrm{K}$). Archival HARPS observations for all targets were obtained from the ESO Archive. Key steps in obtaining the planetary transmission spectrum for each target included performing (and validating) the telluric corrections using `molecfit`, correcting for the planetary and stellar radial velocities during observations, and inverse-variance weighted combination of the spectra to maximise SNR. An empirical Monte Carlo analysis was performed to verify the detection of sodium and to estimate the overall random and systematic error in the detection: we confirmed successful sodium detections at 6.7σ, 3.8σ, and 4.1σ for HD 189733b, WASP 79b and WASP 121b respectively. Gaussian line profiles were fit to the D2 and D1 lines and the best fit line positions, depths, widths were recorded.

The resultant fit parameters (line position, depth and FWHM) prove to be comparable to similar results in the literature. For HD 189733b, the D1 feature parameters are all in good agreement with the literature values; for the D2 line there is good agreement on the line position but poor agreement on the depth and width. This discrepancy is likely due to differences in data reduction: revised results from A. Langeveld, Madhusudhan, and Cabot 2022 for the line depth are -0.39 ± 0.06 % for both the D2 and D1 lines, which are at 1σ agreement with the values measured in this work. For WASP 79b, the only detection in the literature is A. Langeveld, Madhusudhan, and Cabot 2022 which reports line depths of -1.12 ± 0.23 % (D2) and -0.85 ± 0.22 % (D1). This is in 1σ agreement with the values measured in this work. For WASP 121b the values are in good agreement with the literature for both D2 and D1 parameters obtained in this work and confirm that the difficulties in clearly resolving the doublet for WASP 121b are not unique to this work.

The detections of sodium in the upper atmosphere have allowed us to make a number of inferences about the atmospheres for all three targets. We find strong evidence for non-isothermal temperature structure for all three targets, both through considering thermospheric heating and estimating the temperature gradient with altitude. WASP 79b appears to have the strongest thermospheric heating based on the estimates for T_{thermo}, T_1 and T_2. All targets appear to have a negative temperature gradient, which could be interpreted as evidence against thermospheric heating and thermal inversions. This is in tension with the estimates of T_{thermo}, T_1 and T_2 as well as current temperature profile modelling in the literature. Complementing the analysis within this work with low resolution space-based observations would help recover continuum information and allow for more rigorous inferences to made using inverse modelling. All three targets show some evidence of an exosphere with evaporative processes through the measured D2/D1 ratios, particularly WASP 79b and WASP 121b. This is consistent with hydrodynamical simulations in the literature. We find good evidence for all targets of atmospheric winds, but further observations are required to reduce the size of the error bars as the current data quality only allows for broad estimation of the wind speeds.

We identify a number of speculative relationships which could be indicative of broader trends in the hot Jupiters. First, we see that the D2/D1 ratio is strongly negatively correlated with both the escape velocity and the Jeans parameter. Secondly, we observe positive correlation between the planetary surface gravity and the zonal jet speed. Thirdly, we see a positive correlation between the stellar temperature and the day-to-nightside wind. Finally, we observe a negative correlation between the stellar temperature and the cloudiness.

References

Addison, Brett et al. (Sept. 2019). "Minerva-Australis. I. Design, Commissioning, and First Photometric Results". In: *Publications of the Astronomical Society of the Pacific* 131.1005, p. 115003. DOI: 10.1088/1538-3873/ab03aa. URL: https://doi.org/10.1088%2F1538-3873%2Fab03aa.

Allard, N. F. et al. (July 2012). "Theoretical and laboratory spectra of sodium perturbed by molecular hydrogen". In: 543, A159, A159. DOI: 10.1051/0004-6361/201219037.

Astudillo-Defru, N. and P. Rojo (Sept. 2013). "Ground-based detection of calcium and possibly scandium and hydrogen in the atmosphere of HD 209458b". In: 557, A56, A56. DOI: 10.1051/0004-6361/201219018. arXiv: 1306.5475 [astro-ph.EP].

Baxter, Claire et al. (July 2020). "A transition between the hot and the ultra-hot Jupiter atmospheres". In: *Astronomy &amp Astrophysics* 639, A36. DOI: 10.1051/0004-6361/201937394. URL: https://doi.org/10.1051%2F0004-6361%2F201937394.

Ben-Yami, Maya et al. (July 2020). "Neutral Cr and V in the Atmosphere of Ultra-hot Jupiter WASP-121 b". In: 897.1, L5, p. L5. DOI: 10.3847/2041-8213/ab94aa. arXiv: 2006.05995 [astro-ph.EP].

Birkby, J. L. et al. (Nov. 2013). "Detection of water absorption in the day side atmosphere of HD 189733 b using ground-based high-resolution spectroscopy at 3.2μm." In: 436, pp. L35–L39. DOI: 10.1093/mnrasl/slt107. arXiv: 1307.1133 [astro-ph.EP].

Bourrier, V. et al. (Feb. 2013). "Atmospheric escape from HD 189733b observed in H I Lyman-i/i: detailed analysis of HST/STIS September 2011 observations". In: *Astronomy &amp Astrophysics* 551, A63. DOI: 10.1051/0004-6361/201220533. URL: https://doi.org/10.1051%2F0004-6361%2F201220533.

Brogi, Matteo et al. (June 2012). "The signature of orbital motion from the dayside of the planet τ Boötis b". In: 486.7404, pp. 502–504. DOI: 10.1038/nature11161. arXiv: 1206.6109 [astro-ph.EP].

Brown, D. J. A. et al. (Jan. 2017). "Rossiter-McLaughlin models and their effect on estimates of stellar rotation, illustrated using six WASP systems". In: 464.1, pp. 810–839. DOI: 10.1093/mnras/stw2316. arXiv: 1610.00600 [astro-ph.EP].

Cabot, Samuel H. C. et al. (May 2020). "Detection of neutral atomic species in the ultra-hot Jupiter WASP-121b". In: 494.1, pp. 363–377. DOI: 10.1093/mnras/staa748. arXiv: 2001.07196 [astro-ph.EP].

Casasayas-Barris, N., E. Palle, et al. (Dec. 2017). "Detection of sodium in the atmosphere of WASP-69b". In: 608, A135, A135. DOI: 10.1051/0004-6361/201731956. arXiv: 1710.06479 [astro-ph.EP].

Casasayas-Barris, N., E. Pallé, et al. (July 2019). "Atmospheric characterization of the ultra-hot Jupiter MASCARA-2b/KELT-20b". In: *Astronomy &amp Astrophysics* 628, A9. DOI: 10.1051/0004-6361/201935623. URL: https://doi.org/10.1051%2F0004-6361%2F201935623.

Changeat, Q. et al. (May 2022). "Five Key Exoplanet Questions Answered via the Analysis of 25 Hot-Jupiter Atmospheres in Eclipse". In: 260.1, 3, p. 3. DOI: 10.3847/1538-4365/ac5cc2. arXiv: 2204.11729 [astro-ph.EP].

Charbonneau, David et al. (Mar. 2002). "Detection of an Extrasolar Planet Atmosphere". In: 568.1, pp. 377–384. DOI: 10.1086/338770. arXiv: astro-ph/0111544 [astro-ph].

Clough, S. A. et al. (Mar. 2005). "Atmospheric radiative transfer modeling: a summary of the AER codes". In: 91.2, pp. 233–244. DOI: 10.1016/j.jqsrt.2004.05.058.

Crossfield, Ian J. M. and Laura Kreidberg (Dec. 2017). "Trends in Atmospheric Properties of Neptune-size Exoplanets". In: 154.6, 261, p. 261. DOI: 10.3847/1538-3881/aa9279. arXiv: 1708.00016 [astro-ph.EP].

Debrecht, Alex et al. (Feb. 2019). "Photoevaporative flows from exoplanet atmospheres: a 3D radiative hydrodynamic parameter study". In: 483.2, pp. 1481–1495. DOI: 10.1093/mnras/sty3212. arXiv: 1811.09314 [astro-ph.EP].

Ehrenreich, David et al. (June 2015). “A giant comet-like cloud of hydrogen escaping the warm Neptune-mass exoplanet GJ 436b”. In: 522.7557, pp. 459–461. DOI: 10.1038/nature14501. arXiv: 1506.07541 [astro-ph.EP].

Evans, Thomas M. et al. (Aug. 2017). “An ultrahot gas-giant exoplanet with a stratosphere”. In: 548.7665, pp. 58–61. DOI: 10.1038/nature23266. arXiv: 1708.01076 [astro-ph.EP].

Flowers, Erin et al. (May 2019). “The High-resolution Transmission Spectrum of HD 189733b Interpreted with Atmospheric Doppler Shifts from Three-dimensional General Circulation Models”. In: 157.5, 209, p. 209. DOI: 10.3847/1538-3881/ab164c. arXiv: 1810.06099 [astro-ph.EP].

Gebek, Andrea and Apurva V. Oza (Oct. 2020). “Alkaline exospheres of exoplanet systems: evaporative transmission spectra”. In: 497.4, pp. 5271–5291. DOI: 10.1093/mnras/staa2193. arXiv: 2005.02536 [astro-ph.EP].

Haynes, Korey et al. (June 2015). “Spectroscopic Evidence for a Temperature Inversion in the Dayside Atmosphere of Hot Jupiter WASP-33b”. In: 806.2, 146, p. 146. DOI: 10.1088/0004-637X/806/2/146. arXiv: 1505.01490 [astro-ph.EP].

Heng, Kevin (July 2016). “A Cloudiness Index for Transiting Exoplanets Based on the Sodium and Potassium Lines: Tentative Evidence for Hotter Atmospheres Being Less Cloudy at Visible Wavelengths”. In: 826.1, L16, p. L16. DOI: 10.3847/2041-8205/826/1/L16. arXiv: 1606.07218 [astro-ph.EP].

Heng, Kevin et al. (Apr. 2015). “A Non-isothermal Theory for Interpreting Sodium Lines in Transmission Spectra of Exoplanets”. In: 803.1, L9, p. L9. DOI: 10.1088/2041-8205/803/1/L9. arXiv: 1503.05582 [astro-ph.EP].

Hoeijmakers, H. J. et al. (July 2019). “A spectral survey of an ultra-hot Jupiter. Detection of metals in the transmission spectrum of KELT-9 b”. In: 627, A165, A165. DOI: 10.1051/0004-6361/201935089. arXiv: 1905.02096 [astro-ph.EP].

Huitson, C. M. et al. (Apr. 2012). “Temperature-pressure profile of the hot Jupiter HD 189733b from HST sodium observations: detection of upper atmospheric heating”. In: *Monthly Notices of the Royal Astronomical Society* 422.3, pp. 2477–2488. DOI: 10.1111/j.1365-2966.2012.20805.x. URL: https://doi.org/10.1111%2Fj.1365-2966.2012.20805.x.

Kausch, W. et al. (Apr. 2015). “Molecfit: A general tool for telluric absorption correction. II. Quantitative evaluation on ESO-VLT/X-Shooterspectra”. In: 576, A78, A78. DOI: 10.1051/0004-6361/201423909. arXiv: 1501.07265 [astro-ph.IM].

Keles, Engin (Mar. 2021). “Spectral signature of atmospheric winds in high-resolution transit observations”. In: 502.1, pp. 1456–1468. DOI: 10.1093/mnras/stab099. arXiv: 2101.07143 [astro-ph.EP].

Langeveld, Adam, Nikku Madhusudhan, and Samuel H. C. Cabot (May 2022). “A survey of sodium absorption in ten giant exoplanets with high-resolution transmission spectroscopy”. In: *arXiv e-prints*, arXiv:2205.01623, arXiv:2205.01623. arXiv: 2205.01623 [astro-ph.EP].

Langeveld, Adam B et al. (Jan. 2021). “Assessing telluric correction methods for Na detections with high-resolution exoplanet transmission spectroscopy”. In: *Monthly Notices of the Royal Astronomical Society* 502.3, pp. 4392–4404. ISSN: 1365-2966. DOI: 10.1093/mnras/stab134. URL: http://dx.doi.org/10.1093/mnras/stab134.

Lockwood, Alexandra C. et al. (Feb. 2014). “NEAR-IR DIRECT DETECTION OF WATER VAPOR IN TAU BOÖTIS b”. In: *The Astrophysical Journal* 783.2, p. L29. ISSN: 2041-8213. DOI: 10.1088/2041-8205/783/2/l29. URL: http://dx.doi.org/10.1088/2041-8205/783/2/L29.

Madhusudhan, Nikku (Aug. 2019). “Exoplanetary Atmospheres: Key Insights, Challenges, and Prospects”. In: *Annual Review of Astronomy and Astrophysics* 57.1, pp. 617–663. DOI: 10.1146/annurev-astro-081817-051846. URL: https://doi.org/10.1146%2Fannurev-astro-081817-051846.

Mayor, Michel and Didier Queloz (Nov. 1995). “A Jupiter-mass companion to a solar-type star”. In: 378.6555, pp. 355–359. DOI: 10.1038/378355a0.

Meech, Annabella et al. (Mar. 2022). “Applications of a Gaussian process framework for modelling of high-resolution exoplanet spectra”. In: *Monthly Notices of the Royal Astronomical Society* 512.2, pp. 2604–2617. DOI: 10.1093/mnras/stac662. URL: https://doi.org/10.1093%2Fmnras%2Fstac662.

Mikal-Evans, Thomas, David K. Sing, Jayesh M. Goyal, et al. (Sept. 2019). “An emission spectrum for WASP-121b measured across the 0.8-1.1 μm wavelength range using the Hubble Space Telescope”. In: 488.2, pp. 2222–2234. DOI: 10.1093/mnras/stz1753. arXiv: 1906.06326 [astro-ph.EP].

Mikal-Evans, Thomas, David K. Sing, Tiffany Kataria, et al. (Aug. 2020). “Confirmation of water emission in the dayside spectrum of the ultrahot Jupiter WASP-121b”. In: 496.2, pp. 1638–1644. DOI: 10.1093/mnras/staa1628. arXiv: 2005.09631 [astro-ph.EP].

NASA Exoplanet Archive (2022). *NASA Exoplanet Archive*. This research has made use of the NASA Exoplanet Archive, which is operated by the California Institute of Technology, under contract with the National Aeronautics and Space Administration under the Exoplanet Exploration Program. URL: https://exoplanetarchive.ipac.caltech.edu/index.html.

Nugroho, Stevanus K. et al. (Dec. 2017). “High-resolution Spectroscopic Detection of TiO and a Stratosphere in the Day-side of WASP-33b”. In: 154.6, 221, p. 221. DOI: 10.3847/1538-3881/aa9433. arXiv: 1710.05276 [astro-ph.EP].

Perez-Becker, Daniel and Adam P. Showman (Oct. 2013). “Atmospheric Heat Redistribution on Hot Jupiters”. In: 776.2, 134, p. 134. DOI: 10.1088/0004-637X/776/2/134. arXiv: 1306.4673 [astro-ph.EP].

Redfield, Seth et al. (Jan. 2008). “Sodium Absorption from the Exoplanetary Atmosphere of HD 189733b Detected in the Optical Transmission Spectrum”. In: 673.1, p. L87. DOI: 10.1086/527475. arXiv: 0712.0761 [astro-ph].

Seager, Sara and William Bains (2015). “The search for signs of life on exoplanets at the interface of chemistry and planetary science”. In: *Science Advances* 1.2, e1500047. DOI: 10.1126/sciadv.1500047. eprint: https://www.science.org/doi/pdf/10.1126/sciadv.1500047. URL: https://www.science.org/doi/abs/10.1126/sciadv.1500047.

Sedaghati, E. et al. (Nov. 2016). “Potassium detection in the clear atmosphere of a hot-Jupiter. FORS2 transmission spectroscopy of WASP-17b”. In: 596, A47, A47. DOI: 10.1051/0004-6361/201629090. arXiv: 1609.03906 [astro-ph.EP].

Showman, A. P., J. Y. -K. Cho, and K. Menou (2010). “Atmospheric Circulation of Exoplanets”. In: *Exoplanets*. Ed. by S. Seager, pp. 471–516.

Sindel, Jan Philip (2018). “The transmission spectrum of WASP-121b in high resolution with HARPS”. MA thesis. Luleå University of Technology.

Sing, David K. et al. (Aug. 2019). “The Hubble Space Telescope PanCET Program: Exospheric Mg II and Fe II in the Near-ultraviolet Transmission Spectrum of WASP-121b Using Jitter Decorrelation”. In: 158.2, 91, p. 91. DOI: 10.3847/1538-3881/ab2986. arXiv: 1908.00619 [astro-ph.EP].

Smette, A. et al. (Apr. 2015). “Molecfit: A general tool for telluric absorption correction”. In: *Astronomy Astrophysics* 576, A77. ISSN: 1432-0746. DOI: 10.1051/0004-6361/201423932. URL: http://dx.doi.org/10.1051/0004-6361/201423932.

Snellen, Ignas A. G. et al. (June 2010). “The orbital motion, absolute mass and high-altitude winds of exoplanet HD209458b”. In: 465.7301, pp. 1049–1051. DOI: 10.1038/nature09111. arXiv: 1006.4364 [astro-ph.EP].

Steinrueck, Maria E. et al. (July 2019). “The Effect of 3D Transport-induced Disequilibrium Carbon Chemistry on the Atmospheric Structure, Phase Curves, and Emission Spectra of Hot Jupiter HD 189733b”. In: 880.1, 14, p. 14. DOI: 10.3847/1538-4357/ab2598. arXiv: 1808.02011 [astro-ph.EP].

Vidal-Madjar, A. et al. (Nov. 2010). “The Earth as an extrasolar transiting planet. Earth’s atmospheric composition and thickness revealed by Lunar eclipse observations”. In: 523, A57, A57. DOI: 10.1051/0004-6361/201014751. arXiv: 1007.0008 [astro-ph.EP].

Wallack, Nicole L. et al. (Dec. 2019). “Investigating Trends in Atmospheric Compositions of Cool Gas Giant Planets Using Spitzer Secondary Eclipses”. In: 158.6, 217, p. 217. DOI: 10.3847/1538-3881/ab2a05. arXiv: 1908.00014.

Welbanks, Luis et al. (Dec. 2019). “Mass-Metallicity Trends in Transiting Exoplanets from Atmospheric Abundances of H_2O, Na, and K”. In: 887.1, L20, p. L20. DOI: 10.3847/2041-8213/ab5a89. arXiv: 1912.04904 [astro-ph.EP].

Wyttenbach, A. et al. (May 2015). “Spectrally resolved detection of sodium in the atmosphere of HD 189733b with the HARPS spectrograph”. In: 577, A62, A62. DOI: 10.1051/0004-6361/201525729. arXiv: 1503.05581 [astro-ph.EP].

Yan, Dongdong et al. (Feb. 2021). “Atmosphere Escape Inferred from Modeling the Hi/i Transmission Spectrum of WASP-121b”. In: *The Astrophysical Journal* 907.2, p. L47. DOI: 10.3847/2041-8213/abda41. URL: https://doi.org/10.3847%2F2041-8213%2Fabda41.

Yan, Fei and Thomas Henning (July 2018). “An extended hydrogen envelope of the extremely hot giant exoplanet KELT-9b”. In: *Nature Astronomy* 2, pp. 714–718. DOI: 10.1038/s41550-018-0503-3. arXiv: 1807.00869 [astro-ph.EP].